The Pristine Dwarf-Galaxy survey – II. In-depth observational study of the faint Milky Way satellite Sagittarius II

Nicolas Longeard, Nicolas Martin, Else Starkenburg, Rodrigo A. Ibata, Michelle L.M. Collins, Benjamin P.M. Laevens, Dougal Mackey, Robert Michael Rich, David S. Aguado, Anke Arentsen, et al.

Monthly Notices
of the
ROYAL ASTRONOMICAL SOCIETY

MNRAS **491,** 356–377 (2020)
Advance Access publication 2019 October 12

doi:10.1093/mnras/stz2854

The Pristine Dwarf-Galaxy survey – II. In-depth observational study of the faint Milky Way satellite Sagittarius II

Nicolas Longeard,[1★] Nicolas Martin,[1,2] Else Starkenburg,[3] Rodrigo A. Ibata,[1] Michelle L. M. Collins,[4,5] Benjamin P. M. Laevens,[6] Dougal Mackey,[7] R. Michael Rich,[8] David S. Aguado,[9] Anke Arentsen,[3] Pascale Jablonka,[10,11] Jonay I. González Hernández,[12,13] Julio F. Navarro[14] and Rubén Sánchez-Janssen[15,16]

Affiliations are listed at the end of the paper

Accepted 2019 October 4. Received 2019 September 3; in original form 2019 February 7

ABSTRACT

We present an extensive study of the Sagittarius II (Sgr II) stellar system using MegaCam g and i photometry, narrow-band, metallicity-sensitive calcium H&K doublet photometry and Keck II/DEIMOS multiobject spectroscopy. We derive and refine the Sgr II structural and stellar properties inferred at the time of its discovery. The colour–magnitude diagram implies Sgr II is old (12.0 ± 0.5 Gyr) and metal poor. The CaHK photometry confirms the metal-poor nature of the satellite ($[\mathrm{Fe/H}]_{\mathrm{CaHK}} = -2.32 \pm 0.04$ dex) and suggests that Sgr II hosts more than one single stellar population ($\sigma^{\mathrm{CaHK}}_{[\mathrm{FeH}]} = 0.11^{+0.05}_{-0.03}$ dex). Using the Ca infrared triplet measured from our highest signal-to-noise spectra, we confirm the metallicity and dispersion inferred from the Pristine photometric metallicities ($[\mathrm{Fe/H}]_{\mathrm{spectro}} = -2.23 \pm 0.05$ dex, $\sigma^{\mathrm{spectro}}_{[\mathrm{Fe/H}]} = 0.10^{+0.06}_{-0.04}$ dex). The velocity dispersion of the system is found to be $\sigma_v = 2.7^{+1.3}_{-1.0}$ km s^{-1} after excluding two potential binary stars. Sgr II's metallicity and absolute magnitude ($M_V = -5.7 \pm 0.1$ mag) place the system on the luminosity–metallicity relation of the Milky Way dwarf galaxies despite its small size. The low but resolved metallicity and velocity dispersions paint the picture of a slightly dark-matter-dominated satellite ($M/L = 23.0^{+32.8}_{-23.0}$ M$_\odot$ L$_\odot^{-1}$). Furthermore, using the *Gaia* Data Release 2, we constrain the orbit of the satellite and find an apocentre of $118.4^{+28.4}_{-23.7}$ kpc and a pericentre of $54.8^{+3.3}_{-6.1}$ kpc. The orbit of Sgr II is consistent with the trailing arm of the Sgr stream and indicates that it is possibly a satellite of the Sgr dSph that was tidally stripped from the dwarf's influence.

Key words: galaxies: dwarf – Local Group.

1 INTRODUCTION

During the history of the Universe, structures such as galaxies form hierarchically. Therefore, dwarf galaxies (DGs) are particularly old and metal-poor systems and targets of choice to study the history of the local Universe. They are systems spanning a wide range of masses and luminosities. Bright dwarf galaxies such as Sculptor (Shapley 1938b), Draco (Wilson 1955), and Sextans (Irwin et al. 1990) have been known for decades (Mateo 1998), but the extensive search for new dwarf galaxies over the last twenty years has revealed fainter systems (Martin et al. 2006; Zucker et al. 2006b; Belokurov et al. 2007). Still, our knowledge of the Milky Way (MW) satellites remains incomplete. The recent discoveries of several of those faint galaxy candidates with $M_V > -4$ (Willman et al. 2005a; Belokurov et al. 2007; Drlica-Wagner et al. 2015; Laevens et al. 2015b; Luque et al. 2016) are promising as they might well bring new perspectives to near-field cosmology (Bullock & Boylan-Kolchin 2017).

The study of these nearby small-scale structures can allow one to explore various problematics in astrophysics, from the faint end of the galaxy luminosity function (Koposov et al. 2009) to the validity of cosmological models. Therefore, DGs are important cosmological probes (Pawlowski et al. 2017; Tulin & Yu 2017) as the comparison of their observed properties with the predictions made by current lambda cold dark matter (ΛCDM) models leads to some discrepancies that we have to understand in order to constrain and refine our cosmological models. For example, the number of faint satellites, their distribution in the sky, and their stellar masses and mass profiles are still in tension with ΛCDM (Navarro et al. 2010; Boylan-Kolchin, Bullock & Kaplinghat 2011; Pawlowski, McGaugh & Jerjen 2015). DGs are also thought to be among the most dark matter (DM hereafter) dominated systems in the Universe

★ E-mail: nicolas.longeard@astro.unistra.fr

(Wolf et al. 2010) and could be useful for the detection of the elusive DM particle through self-annihilation processes (Bertone, Hooper & Silk 2005; Geringer-Sameth, Koushiappas & Walker 2015).

However, using faint dwarf galaxies as cosmological probes can be challenging as their exceptional faintness comes with observational challenges. The overall properties and/or even the very nature of the recently discovered systems can sometimes be puzzling as the distinction between galaxy and globular cluster is difficult to make (e.g. Conn et al. 2018; Longeard et al. 2018). Therefore, only the combined efforts of deep photometric surveys, such as the Dark Energy Survey (DES; The Dark Energy Survey Collaboration 2005), the Panoramic Survey Telescope and Rapid Response System (PS1; Chambers et al. 2016), and the Sloan Digital Sky Survey (SDSS York et al. 2000), and spectroscopic observations can hope to improve our understanding on the faint end of the luminosity function and the history of the Milky Way.

In this context, we present here a study of the MW satellite Sagittarius II (Sgr II), discovered by Laevens et al. (2015a; hereafter L15) in PS1, where it was identified as an old (12.5 Gyr) and metal-poor ([Fe/H] $= -2.20$ dex) dwarf-galaxy candidate. L15 noticed that Sgr II had a peculiar location on the sky: Its position and distance were found to be consistent with the predictions of models for the Sagittarius stream (Law & Majewski 2010). They concluded that this satellite might actually have been a satellite of the bright Sagittarius dwarf galaxy discovered by Ibata, Gilmore & Irwin (1994), deposited in the MW's halo as its host is being tidally destroyed. However, spectroscopic observations were still needed at the time to dynamically tie the stream and Sgr II, as well as confirming the galaxy nature of the satellite. Sgr II was also recently studied by Mutlu-Pakdil et al. (2018, M18) with *Magellan*/MegaCam photometry and they confirmed the structural properties inferred by L15. Furthermore, using both blue horizontal branch (BHB) stars and a CMD-fitting technique, they constrained it to host an old (13.5 Gyr), metal-poor ([Fe/H] $= -2.2$ dex) stellar population, with an alpha abundance ratio of α/Fe $=$0.4 dex, and a distance modulus $m - M = 19.2 \pm 0.2$ mag. Moreover, they found a half-light radius of 32 ± 1.0 pc, and an absolute magnitude of $M_V = -5.2 \pm 0.1$ mag. Based on all these photometric properties, M18 concluded that the system is likely a globular cluster, and compared the satellite to several extended clusters of M31 associated with known streams, in the same way that Sgr II is suspected to be linked to the Sgr stream. However, M18 emphasized the importance of a spectroscopic study to confirm their conclusion.

In this work, we present a thorough analysis of the stellar, structural, and orbital properties of Sgr II using deep broad-band photometry from the Canadian–France–Hawaii Telescope (CFHT) MegaCam (MC) imager in the context of the Pristine survey. The Pristine survey uses a narrow-band filter centred on the metallicity-sensitive Ca H&K doublet (Starkenburg et al. 2017) to identify metal-poor stars and estimate their metallicity using pure photometry. Keck II/DEIMOS spectroscopy is additionally used to constrain the system's metallicity and kinematics. Finally, combined with the *Gaia* Data Release 2, we constrain the orbital properties of the satellite.

2 OBSERVATIONS AND DATA

2.1 Photometry

Our photometry consists of deep broad-band g_{MC} and i_{MC} observations as well as narrow-band observations with the CaHK filter centred on the metallicity-sensitive Calcium H&K doublet. Sgr II was observed using the wide-field imager MegaCam on the CFHT (Boulade et al. 2003). The CaHK photometry is part of a larger survey called Pristine (Starkenburg et al. 2017).

Observations were conducted in service mode by the CFHT staff during the night of 2016 July 2, under good seeing conditions ($\sim$0.4 arcsec). The integration times are of 3×700 s in g_{MC}, 5×500 s in i_{MC}, and 3×705 s in CaHK. We refer the reader to Laevens et al. (2015b; hereafter L18) for the details of the MegaCam data reduction. The star/galaxy separation is done using the Cambridge Astronomical Survey Unit (Irwin & Lewis 2001) pipeline flags, which also indicate saturated sources. The MegaCam photometry is calibrated on to the PS1 photometric system following the same procedure as in L18: A cross-identification of all unsaturated point sources with photometric uncertainties below 0.05 mag in both catalogues is performed. The difference $g_{MC} - g_{PS1}$ (respectively $i_{MC} - i_{PS1}$) is expressed as a function of the colour $g_{MC} - i_{MC}$. We then fit a third-order polynomial to translate MC photometry into PS1 through a 3σ clipping procedure. The coefficients of the polynomials to transform (g_{MC}, i_{MC}) into (g_{PS1}, i_{PS1}) in this work are different from those in L18 because the uncalibrated colour $g_{MC} - i_{MC}$ differs. We define $x \equiv g_{MC} - i_{MC}$ and obtain:

$$g_{MC} - g_{P1} = a_0^g x^2 + a_1^g x + a_2^g,$$
$$i_{MC} - i_{P1} = a_0^i x^2 + a_1^i x + a_2^i.$$

The calibration coefficients are $a_0^g = -0.0162 \pm 0.0046$, $a_1^g = 0.0906 \pm 0.0029$, $a_2^g = -0.0696 \pm 0.0016$ for the g band and $a_0^i = -0.0117 \pm 0.0032$, $a_1^i = 0.0058 \pm 0.0022$, $a_2^i = -0.1359 \pm 0.0010$ for the i band. All uncertainties on the polynomials coefficients are propagated into the photometric uncertainties.

All stars saturated in the MC photometry, filtered during the calibration process, are taken directly from PS1 and added to the final catalogue, for a total of 83 355 stars. This catalogue is finally dereddened using the dust map from Schlegel, Finkbeiner & Davis (1998) and the extinction coefficients from Schlafly & Finkbeiner (2011). In the rest of the text, we use the combined catalogue and the PS or MC subscripts are dropped. The 50 per cent completeness of the data is reached at $g_0 \sim 24.2$ and $i_0 \sim 23.4$ mag.

2.2 Spectroscopy

Spectroscopic follow-up observations of Sgr II were obtained with Keck and the Deep Extragalactic Imaging Multi-Object Spectrograph (DEIMOS) (Faber et al. 2003). Similarly to L18, the standard set-up was used here with the OG550 filter and the 1200 lines mm^{-1} grating. The wavelength range goes from 6500 to 9000 Å, for a resolution of $\sim$8500. 'Mask 1' was observed on 2015-09-12 and reobserved on 2015-09-18 (97 stars) and 'mask 2' on 2015-09-08 (110 stars). Mask 2 was designed to be perpendicular to the other two in order to probe potential Sgr II members further away in the South/North direction (Fig. 1). Stars observed spectroscopically were selected based on their distance from the Sgr II population in the CMD as identified by Laevens et al. (2015a). The velocities were derived by selecting a slitmask in the package IRAF SIMULATOR provided by the Keck Observatories, and the pipeline of Ibata et al. (2011). The latter compares a template created from the calcium II triplet features at rest added to a continuous stellar spectrum with the observed spectra to fit for the Doppler shift with a Monte Carlo Markov Chain (MCMC; Hastings 1970) algorithm. This MCMC procedure gives a probability distribution function (PDF) of the radial velocity, from which the velocity uncertainty is measured.

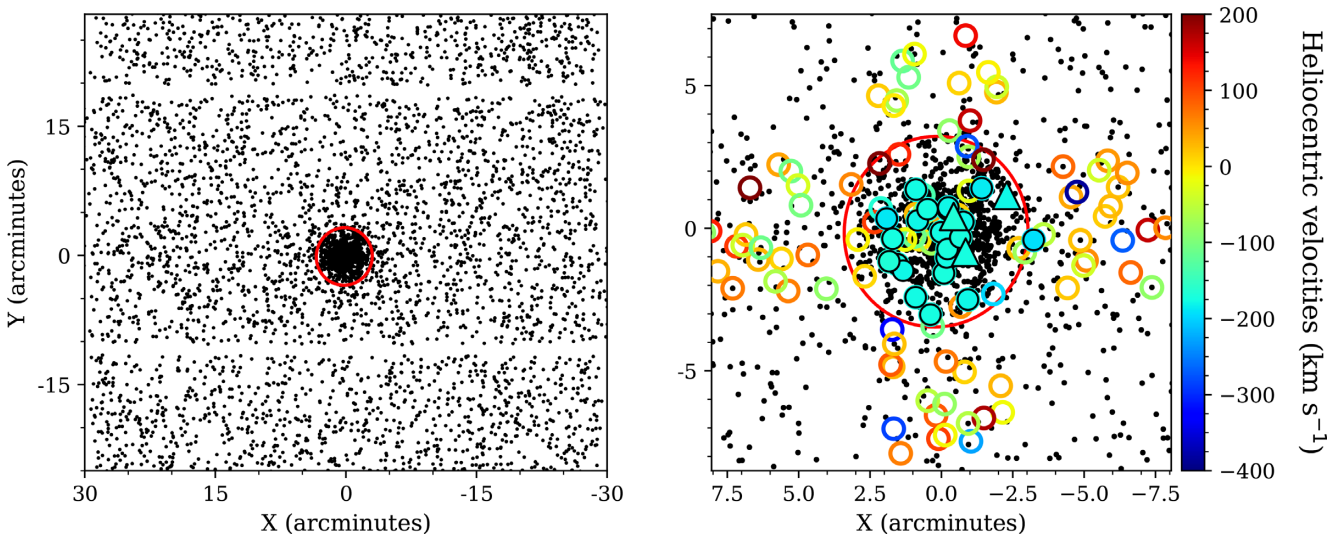

Figure 1. *Left-hand panel:* spatial distribution of Sgr II-like stars, i.e. stars with a CMD probability membership of 10 per cent or higher. The field is centred on ($\alpha_0 = 298.16628°$, $\delta_0 = -22.89633°$). The red contour defines the two half-light radii ($r_h \sim 1.7$ arcmin) of the satellite. *Right-hand panel:* close-up on the central region, with stars observed spectroscopically colour-coded according to their heliocentric velocities. Filled circles represent stars spectroscopically confirmed as Sgr II members, while filled triangles represent Sgr II HB stars in the spectroscopic data set.

The typical velocity uncertainty of our data is of order ~ 3 km s^{-1} at signal-to-noise ratio (S/N) = 12.

All stars with an S/N below 3 or with a velocity uncertainty greater than 15 km s^{-1} are discarded, resulting in a final spectroscopic sample of 118 stars. Following the procedure described in Simon & Geha (2007) and using the 47 stars observed at least twice and that pass the S/N and velocity uncertainty cuts, we assess the systematics in our sample, including the wavelength calibration uncertainty, and find a negligible bias of 0.4 ± 1.3 km s^{-1} and a systematic uncertainty floor of $\delta_{\rm thr} = 1.8^{+0.3}_{-0.2}$ km s^{-1}. The heliocentric velocities of the stars observed more than once are combined by taking the mean of all available quantities weighted by the inverse of their respective velocity uncertainties. The same procedure is followed for the equivalent widths of the Ca triplet.

Finally, the existence of binaries in the sample is investigated for all stars with multiple velocity measurements. To do so, we define the quantity μ such that

$$\mu = \frac{v_{r,l} - v_{r,m}}{\sqrt{\delta^2_{vr,l} + \delta^2_{vr,m} + 2\delta^2_{\rm thr}}},$$

with $v_{r,l}$ (resp. for $v_{r,m}$) the heliocentric velocity of a star in mask l (resp. mask m), and $\delta_{vr,l}$ (resp. $\delta_{vr,m}$) the uncertainty on this measurement. If μ is greater than 2.5 (a '2.5σ deviation' between the two velocity measurements), the star is considered a potential binary and flagged accordingly. Two stars are identified as such through this procedure, with differences in velocities of 21.46 ± 6.75 and 25.07 ± 7.91 km s^{-1}. This variation over one week is large but has been observed before in the dwarf galaxy Bootes I (Koposov et al. 2011).

3 BROAD-BAND PHOTOMETRY ANALYSIS

We present the one square degree field centred on Sgr II together with the spatial distribution of stars observed with spectroscopy in Fig. 1.

The CMD of all stars within two half-light radii ($r_h \sim 1.7$ arcmin) of the system is shown in the left-hand panel of Fig. 2, along with the spectroscopically observed stars. The CMD of the same areal coverage but selected in the outskirts of the MegaCam field of view is represented as a comparison in the middle panel. The main-sequence (MS) and MS turn-off (MSTO) of Sgr II are very well defined thanks to the depth of the MegaCam data, and correspond to an old (>12 Gyr) and very metal-poor ([Fe/H] < −2.0) population. A few blue stragglers can be seen in the satellite. Sgr II also hosts a few blue horizontal branch stars at $g_0 \sim 19.7$.

The BHB stars are useful as they are good distance tracers (Deason, Belokurov & Evans 2011; hereafter D11) so we start by using them to measure the distance to Sgr II. Two out of the three BHBs that were observed with spectroscopy are not compatible with the systemic velocity of Sgr II (see Section 5). They are therefore discarded. The remaining 10 BHBs' g_0 and r_0 are calibrated on to the SDSS photometry according to the colour equations of Tonry et al. (2012). Relation (7) of D11 that allows us to find the absolute magnitude of BHBs only holds for stars in the colour interval $-0.25 < (g-r)_{0,\rm SDSS} < 0.0$. For this reason, another star is rejected from the sample. Using this relation for the nine remaining stars yields $M_g = 0.47 \pm 0.02$ mag and a median distance modulus of $(m - M)_{\rm BHB} = 19.19 \pm 0.10$ mag or 68.8 ± 3.0 kpc.

3.1 Structural and CMD fitting

We use our MC photometry to refine the structural properties of Sgr II previously studied by L15 and M18 and determine its main stellar properties through a CMD and spatial distribution fitting procedure. The formalism of this analysis is detailed in Martin et al. (2016a) and L18. Though the main steps will be briefly detailed below, we refer the reader to these two references for more details. Six structural parameters are inferred from our analysis: the centroid offsets along the X and Y axes with respect to the centre coordinates of the literature, x_0 and y_0, the ellipticity ϵ,[1] the half-light radius r_h, the position angle θ, and the number of stars N^* of the satellite.

[1]The ellipticity is defined as $1 - \frac{a}{b}$, with a and b the major and minor axis extent of the system.

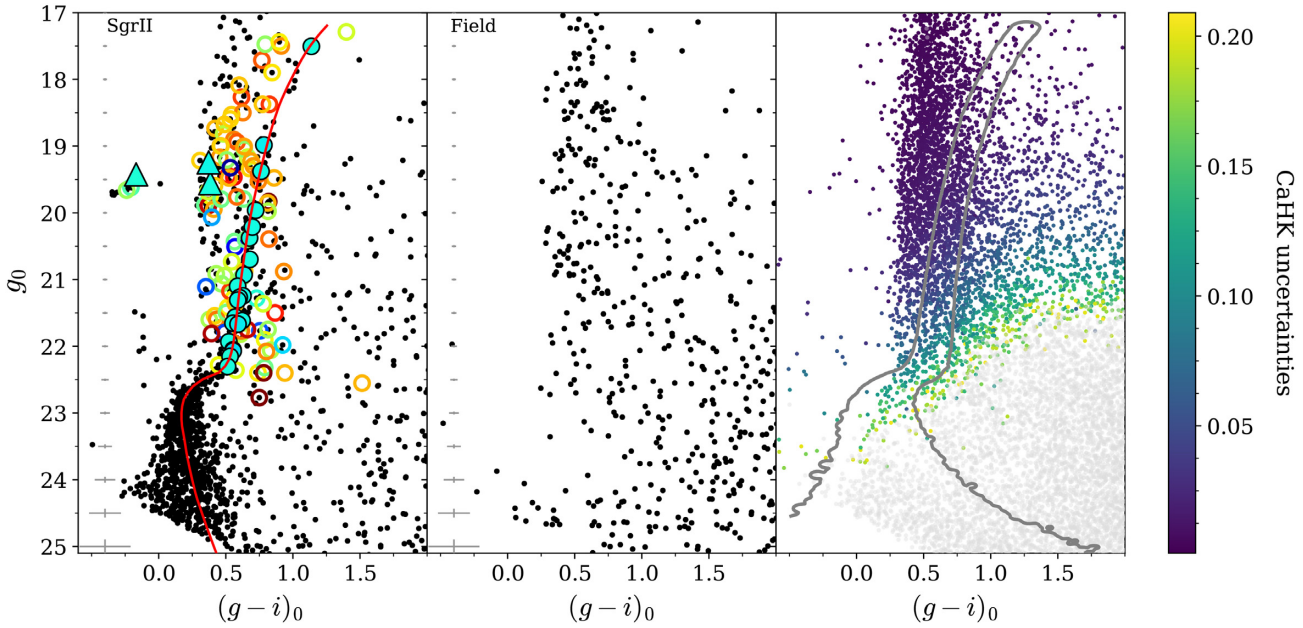

Figure 2. *Left-hand panel:* CMD within two r_h of Sgr II. Its old (>10 Gyr) and metal-poor ([Fe/H] < −2.2) stellar population clearly stands out. One can notice the presence of a few blue stragglers in the system around $g_0 \sim 22.0$, as well as the Sgr II horizontal branch. Stars observed with spectroscopy are shown with coloured circles. The colour scheme used in this panel is the same as the one in Fig. 1. The filled ones represent the confirmed spectroscopic members. Filled triangles show the location, in the CMD, of HB stars in the spectroscopic data set. The favoured isochrone for Sgr II, obtained in Section 3, is shown as a solid red line (12 Gyr, [Fe/H] = −2.35 dex, α/Fe = 0 dex, $m - M$ =19.32 mag). *Middle panel:* CMD of the field for an equivalent centred on ($X = -12$, $Y = -12$) arcmin. *Right-hand panel:* photometric uncertainties for the CaHK band. The grey contours show the mask used to select the Sgr II-like population showed in the spatial distribution of Fig. 1.

These structural properties are gathered in a parameter set noted $\mathcal{P}_{\rm spac} \equiv \{x_0, y_0, \epsilon, r_{\rm h}, \theta, N^*\}$.

We then define the CMD parameters derived by our CMD fitting procedure: the age of the satellite A, the systemic metallicity $[{\rm Fe/H}]_{\rm CMD}$, the [α/Fe] abundance ratio, the distance modulus $m - M$, and η the fraction of Sgr II stars with respect to the total number of stars in the field chosen for the analysis. We regroup these properties into the set $\mathcal{P}_{\rm CMD} \equiv \{A, [{\rm Fe/H}]_{\rm CMD}, [\alpha/{\rm Fe}], m - M, \eta\}$.

For a given star k, we consider its following properties: its $g_{\rm k}$ and $i_{\rm k}$ magnitudes, and its position offset from the centre coordinates of the literature, X_k and Y_k. These four properties are gathered into one set $\vec{d_k} = \{X_k, Y_k, g_k, i_k\}$.

The Sgr II radial density, $\rho_{\rm dwarf}$, is modelled by the following exponential radial profile:

$$\rho_{\rm dwarf}(r) = \frac{1.68^2}{2\pi r_{\rm h}^2(1-\epsilon)} \exp\left(-\frac{1.68r}{r_{\rm h}}\right), \quad (1)$$

with r the elliptical radius, which can be expressed using the projected sky coordinates (x, y) as

$$r = \left(\left(\frac{1}{1-\epsilon} \Big((x-x_0)\cos\theta - (y-y_0)\sin\theta \Big) \right)^2 + \Big((x-x_0)\sin\theta + (y-y_0)\cos\theta \Big)^2 \right)^{1/2}. \quad (2)$$

For the kth star, the spatial likelihood can then simply be written as

$$\ell_{\rm sp}^{\rm SgrII}(X_k, Y_k) = \frac{\rho_{\rm dwarf}(r)}{\int_S \rho_{\rm dwarf}(r) {\rm d}S}, \quad (3)$$

where S is in the area of the sky over which the analysis is conducted.

The spatial likelihood of the Milky Way foreground contamination is assumed flat over the field of view, which yields

$$\ell_{\rm sp}^{\rm MW} = \frac{1}{\int {\rm d}S}. \quad (4)$$

The CMD likelihood function $\ell_{\rm CMD}$ is built from the sum of two models: one for the foreground, $\ell_{\rm CMD}^{\rm MW}$, constructed empirically from the field CMD, and one to describe the Sgr II population taken as a single stellar population, and called $\ell_{\rm CMD}^{\rm SgrII}$. The foreground contamination model is built by selecting all stars outside $5r_{\rm h}$ of the system centre and binning their distribution on the CMD. This distribution is smoothed by a Gaussian kernel in both colour and magnitude of a width of 0.1 in an attempt to limit the effects of shot noise. $\ell_{\rm CMD}^{\rm SgrII}$ is generated using a range of Darmouth isochrones (Dotter et al. 2008). We choose isochrones of different $[{\rm Fe/H}]_{\rm CMD}$, A, [α/Fe], and distance modulus $m - M$. The priors on each parameters are reported in Table 1. To build the PDF of a given stellar population, we simulate the CMD of a population of several million stars, based on its isochrone, luminosity function, and photometric uncertainty at a given (g_0, i_0). To avoid aliasing effects, especially at the bright end of our models where the photometric uncertainties are unrealistically low, we add 0.01 in quadrature to the photometric uncertainties. Finally, each PDF is degraded by the completeness of the data, estimated following the method of Martin et al. (2016a).

The structural and CMD parameters are gathered into a single set $\mathcal{P} \equiv \{A, [{\rm Fe/H}], [\alpha/{\rm Fe}], \mu, \epsilon, r_{\rm h}, x_0, y_0, \theta, \eta\}$. At the distance of Sgr II, the tip of the red giant branch (RGB) is expected to be located at $g_0 \sim 17.0$. Furthermore, misidentified background galaxies start to pollute our photometry below $g_0 \sim 25.0$. The fit does not take into account the horizontal branch stars as these are poorly modelled by the theoretical stellar population models. Therefore, the analysis is restricted in a specific CMD box defined with the following cuts:

Table 1. Properties of Sgr II.

Parameter	Unit	Prior	Favoured model	Uncertainties
Right ascension (ICRS) α	degrees	–	298.16628	±0.001
Declination (ICRS) δ	degrees	–	−22.89633	±0.001
l	degrees	–	18.93203	±0.001
b	degrees	–	−22.89461	±0.001
$r_{\rm h}$	arcmin	>0	1.7	±0.05
r_h	pc		35.5	$^{+1.4}_{-1.2}$
θ	degrees	[0,180]	103	$^{+28}_{-17}$
ϵ	–	[0, 1]	0.0	<0.12 at the 95% CL
Distance modulus	mag	[18.90,19.45]	19.32	$^{+0.03}_{-0.02}$
Distance	kpc		73.1	$^{+1.1}_{-0.7}$
A	Gyr	[9,13.5]	12.0	± 0.5
[Fe/H]	dex	[−2.4,−1.5]	−2.28	± 0.03
[α/Fe]	dex	[−0.2,0.6]	0.0	±0.2
log(Luminosity)	–	>0	4.20	±0.1
M_V	mag	–	−5.7	± 0.1
μ_0	mag arcsec^{-2}	–	24.7	±0.2
$<v_r>$	km s^{-1}	–	−177.3	±1.2
σ_{vr}	km s^{-1}	> 0	2.7	$^{+1.3}_{-1.0}$
μ^*_α	mas yr^{-1}	–	−0.65	$^{+0.08}_{-0.10}$
μ_δ	mas yr^{-1}	–	−0.88	±0.12
Apocentre	kpc	–	118.4	$^{+28.4}_{-23.7}$
Pericentre	kpc	–	54.8	$^{+3.3}_{-6.1}$
$\epsilon_{\rm orbit}$	–	>0	0.44	±0.01
U	km s^{-1}	–	0.4	$^{+14.1}_{-19.5}$
V	km s^{-1}	–	−366.5	$^{+27.3}_{-42.8}$
W	km s^{-1}	–	160.3	$^{+26.3}_{-19.9}$
L_z	km s^{-1} kpc	–	6292	$^{+2236}_{-1899}$
E	km^2 s^{-2}	–	17 159	$^{+10\,213}_{-3120}$

$-0.2 < g_0 - i_0 < 1.2$ and $17.0 < g_0 < 25.0$. CMD and spatial properties are fitted at the same time through our own MCMC algorithm by maximizing the likelihood of the following model:

$$\mathcal{L}_{\rm tot} = \sum_{k=1}^{N} \ell_{\rm tot}(\vec{d}_k|\mathcal{P}) = \eta \ell_{\rm SgrII}(\vec{d}_k|\mathcal{P}) + (1-\eta)\ell_{\rm MW}(\vec{d}_k), \quad (5)$$

with

$$\ell_{\rm SgrII}(\vec{d}_k|\mathcal{P}) = \ell^{\rm SgrII}_{\rm CMD}(g_k, i_k|\mathcal{P}_{\rm CMD})\ell^{\rm SgrII}_{\rm sp}(X_k, Y_k|\mathcal{P}_{\rm spac}), \quad (6)$$

$$\ell_{\rm MW} = \ell^{\rm MW}_{\rm CMD}(g_k, i_k)\ell^{\rm MW}_{\rm sp}(X_k, Y_k). \quad (7)$$

Finally, the distance to Sgr II is constrained using a Gaussian prior based on the distance modulus derived from the median absolute magnitude of the BHBs in the first paragraph of Section 3 ($m - M = 19.19 \pm 0.10$ mag). A Gaussian prior on the metallicity of the satellite is also applied and comes directly from the combination of the spectroscopic and CaHK metallicity measurements detailed in Sections 4 and 5 respectively ([Fe/H]$_{\rm SgrII} = -2.28 \pm 0.03$ dex). The inference of each parameter of $\mathcal{P}$ is summed up in Table 1, and the 2D PDFs are shown in Fig. 3.

The best-fitting isochrone is shown as the red PDFs in Fig. 3. Sgr II is found to be significantly old and metal-poor, with an age of 12.0 ± 0.5 Gyr, along with a systemic metallicity of -2.35 ± 0.05 dex. Furthermore, the alpha abundance of this isochrone is solar ([α/Fe] = 0.0), though we caution the reader about reading too much into this parameter given the roughness of the [α/Fe] abundance ratio grid. Finally, the favoured distance modulus is $\mu = 19.32^{+0.03}_{-0.02}$ mag, and corresponds to a physical distance of $73.1^{+1.1}_{-0.7}$ kpc. We compare these results by performing the fit without the BHBs or the spectroscopic metallicity priors. For this case, the PDFs are shown in black in Fig. 3. The inferences of all the parameters are compatible: The stellar population is here found to be older (12.5 ± 0.5 Gyr) and the metallicity reaches the lower edge of the metallicity grid. In this case, the analysis only gives an upper limit on the metallicity of [Fe/H] = −2.45 dex. The distance modulus is found to be $m - M = 19.35 \pm 0.05$ mag. All structural properties are perfectly compatible with L15 and M18. Sgr II is consistent with being spherical ($\epsilon < 0.12$ at the 95 per cent confidence limit) and has a size of $r_{\rm h} = 1.70 \pm 0.05$ arcmin, translating into a physical half-light radius of $35.5^{+1.4}_{-1.2}$ pc. All the main properties of Sgr II are summarized in Table 1.

Finally, we investigate the presence of RR Lyrae in the field by cross-identifying the PS1 RR Lyrae catalogue of Sesar et al. (2017, S17) with our photometry. Three RR Lyrae are found in the vicinity of Sgr II. Two of these have similar distance modulii, as inferred from S17 (18.73 and 18.85 mag). However, the resulting distances are discrepant from both our BHB and CMD fitting analyses by 0.5 mag (roughly 10 kpc in physical distance). To confirm the distance modulus of Sgr II, we compare the CMD of the satellite with fiducials of MW globular clusters in PS1 (Bernard et al. 2014) in Fig. 4. In this plot, all fiducials are deredenned and their distance modulii are corrected to correspond to the mean RR Lyrae distance

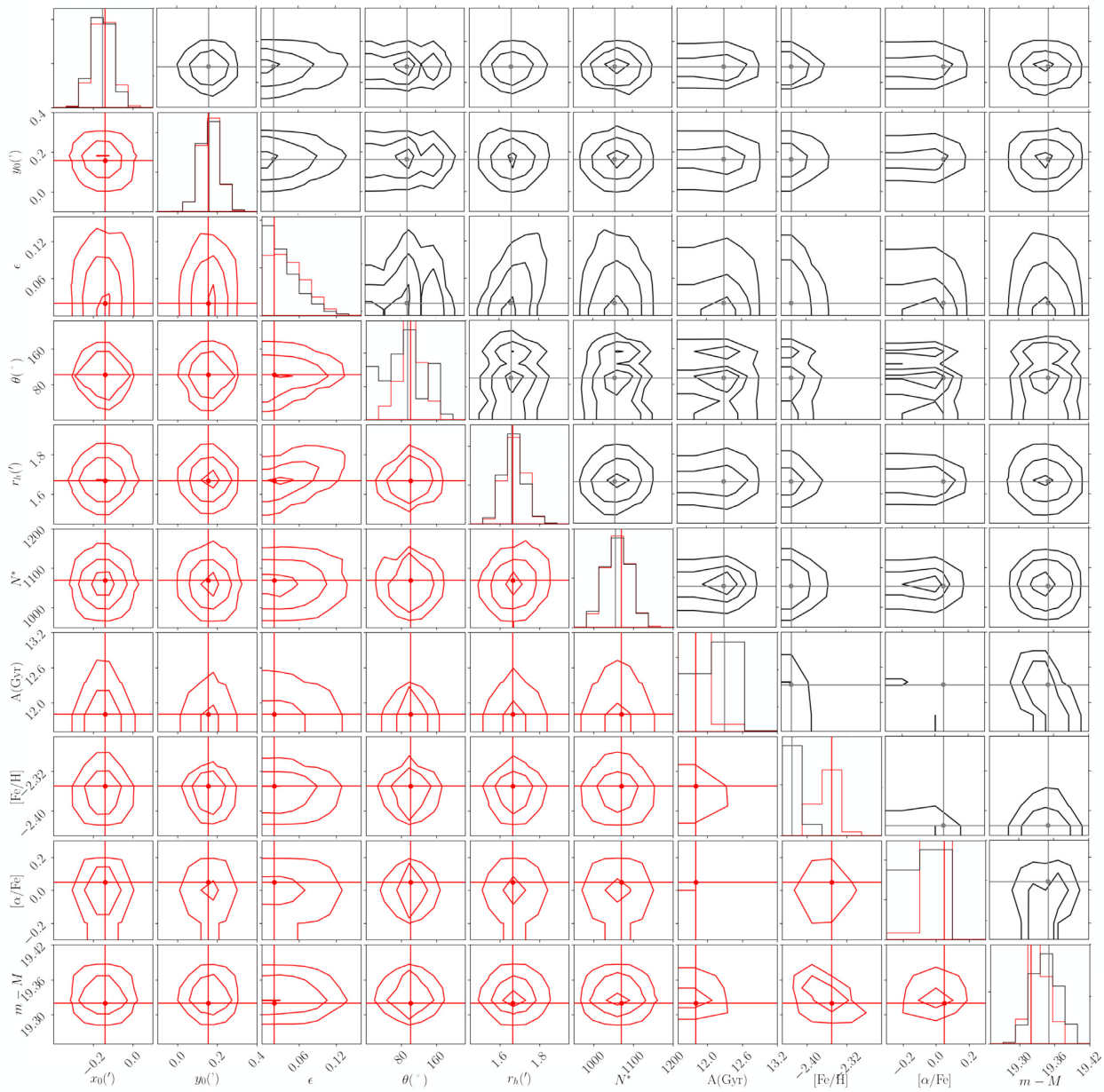

Figure 3. One and two-dimensional PDFs of the structural and CMD properties of Sgr II, inferred using the method described in Section 3.1. Red lines correspond to the favoured inference, using both the distance prior based on BHBs and the metallicity prior from the spectroscopy, while the black contours show the case without any prior. These contours are defined as the usual 1, 2, and 3σ confidence intervals in the 2D, Gaussian case. This figure shows that using the distance and metallicity priors has a limited impact on our final results. The structural properties remain unchanged in both cases and indicate that Sgr II is spherical with a half-light radius of ∼1.7 arcmin. The CMD properties are consistent and show that the satellite is old, metal-poor, and more distant than previously estimated by Laevens et al. (2015a) (∼73.1 kpc).

($m - M = 18.79$ mag) in the left-hand panel, and to our favoured model for Sgr II ($m - M = 19.32 \pm 0.03$ mag) in the right-hand one. For the RR Lyrae distance, the features of Sgr II are well reproduced by the light green fiducials with a metallicity between −1.8 and −1.4 dex. The spectroscopic members shown as yellow diamonds also follow nicely the light green tracks. At the favoured model distance, the dark blue, more metal-poor fiducials are a better description of the CMD of the satellite and its members. However, both the CaHK photometry and the spectroscopy (see Sections 4 and 5) show that Sgr II is very metal-poor ([Fe/H] ∼ −2.3 dex). Therefore, the distance found from the RR Lyrae is clearly not that of Sgr II. A plausible origin for these two stars might just be the Sgr stream, as shown in Section 6.

Another distance measurement based on RR Lyrae in the Sgr II field has recently been proposed by Joo et al. (2019, J19). Using their own method, they find a distance modulus of 19.03 ± 0.10 mag using five RR Lyrae. After investigations, we found three RR Lyrae in common between the catalogue of S17 and J19. Only one of those is an RRab star with a reliable distance measurement in S17 of $m - M \sim 18.85$ mag. It appears that distance modulus inferences between the two catalogues do not agree with each other. One of the sources of disagreement could lie in the extinction used, which

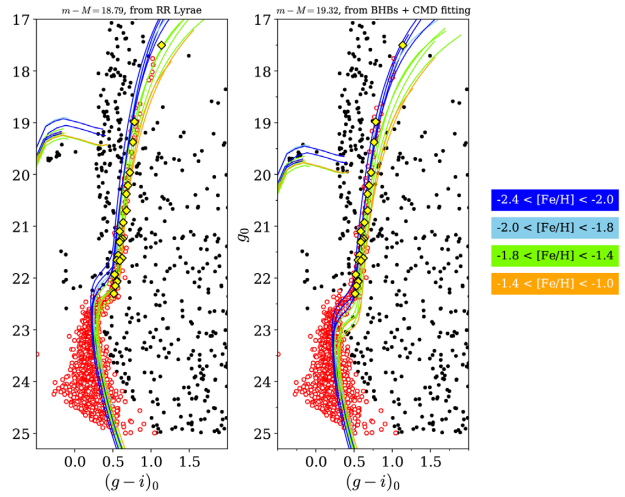

Figure 4. CMDs within two half-light radii of Sgr II overplotted with the fiducials of MW globular clusters from Bernard et al. (2014) shifted at two different distance modulii, one inferred from the RR Lyrae in the field ($m - M = 18.79$ mag) on the left and one from the BHBs and CMD fitting on the right ($m - M = 19.32$ mag). Stars with a Sgr II membership probability greater than ten per cent from the broad-band photometry analysis are shown as red circles. Spectroscopically confirmed members of Sgr II are shown as yellow diamonds. The fiducials are separated in metallicity bins, from the most metal-poor in dark blue to the most metal-rich available in orange.

is twice as large in the catalogue of S17. This issue is also raised by J19. Repeating the CMD and structural analysis with this $m - M$ also yields compatible results in terms of size and luminosity, while the satellite is found older is this case (13.5 ± 0.5 Gyr). None the less, reproducing Fig. 4 with this other distance modulus measurement still does not reproduce the different features of the CMD of Sgr II well, especially the BHB. We therefore favour our distance modulus inference for the rest of this work.

3.2 Luminosity

The luminosity, absolute magnitude, and surface brightness of Sgr II are derived using the formalism of Martin et al. (2016a). The first step consists in drawing a set of parameters denoted j from the final multidimensional PDF obtained through the analysis of Section 3.1. These parameters are the number of stars N^*_j, an age A_j, the metallicity $[\mathrm{Fe/H}]^{\mathrm{CMD}}_j$, the alpha abundance ratio $[\alpha/\mathrm{Fe}]_j$, and the distance modulus $(m - M)_j$. A CMD of the jth stellar population is then simulated. For each simulated star, we ensure that its location in the CMD falls in the CMD box used to perform the structural and CMD fit ($-0.2 < g_0 - i_0 < 1.2$ and $17.0 < g_0 < 25.0$). Furthermore, a completeness test is performed: The completeness of the survey is first estimated at the colour and magnitude of the simulated star. Then, two random numbers a and b between 0 and 1 are drawn: If the completenesses of the star in both g and i is greater than these numbers, it is flagged. When the number of flagged stars reaches N^*_j, the fluxes of all simulated stars, flagged or not, are summed, which gives the luminosity L_j of the satellite for the jth iteration. This procedure is repeated a thousand times in order to correctly sample the PDFs.

The 1D marginalized PDFs of Sgr II's luminosity and absolute magnitude M_V are represented in Fig. 5. The final favoured parameters are reported in Table 1. The luminosity of the satellite is inferred to be $\log(L_V) = 4.2 \pm 0.1$. This measurement is in agreement with

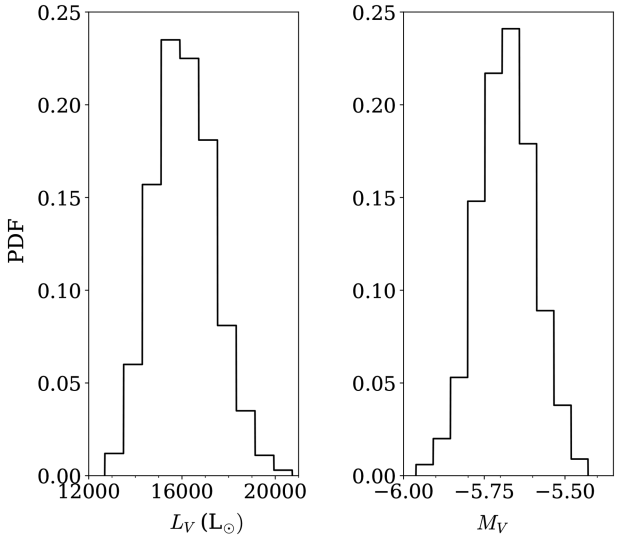

Figure 5. PDFs of the Sgr II luminosity and absolute magnitude. The favoured luminosity of the satellite is $\log(L_V) = 4.2 \pm 0.1$, corresponding to an absolute magnitude of $M_V = -5.7 \pm 0.1$ mag.

both L15 and M18 ($\log(L_V) = 4.1 \pm 0.1$). Finally, we obtain a surface brightness of $S_0 = 24.7 \pm 0.2$ mag arcsec^{-2}.

4 NARROW-BAND CAHK PHOTOMETRY ANALYSIS

Our CaHK photometry is provided by the Pristine Survey that uses a narrow-band filter centred on the metallicity-sensitive calcium H&K doublet lines. Therefore, the flux received in this filter depends on the metallicity of the observed stars. By combining the CaHK_0 magnitudes with the broad-band g_0 and i_0 photometry, the photometric metallicity of each star can be estimated. More details on the Pristine survey and the model used to transform (CaHK_0, g_0, i_0) into a photometric metallicity can be found in Starkenburg et al. (2017). Pristine observations are shallower than our broad-band g and i photometry (right-hand panel of Fig. 2) and therefore can only be used to estimate the photometric metallicity $[\mathrm{Fe/H}]_{\mathrm{CaHK}}$ of stars in our field down to $g_0 \sim 23$ mag. This limit corresponds to a CaHK photometric uncertainty of ∼0.1 mag. Above this value, the resulting photometric metallicities are less reliable.

Starkenburg et al. (2017) shows that the Pristine metallicities are slightly biased low as we go towards the metal-poor end of the calibration model. Therefore, we repeat the procedure presented in L18 and we first correct for this effect by binning in metallicity the sample used by Starkenburg et al. (2017), which provides both the SDSS spectroscopic metallicity and the Pristine photometric metallicity for several thousand stars. For each bin, the median difference between the SDSS and Pristine metallicities is computed. This procedure yields the bias as a function of the photometric metallicity, which is used to correct our whole Sgr II metallicity catalogue. All stars with $[\mathrm{Fe/H}]_{\mathrm{CaHK}} < -4.0$ or $[\mathrm{Fe/H}]_{\mathrm{CaHK}} > -1.0$ are discarded as our Pristine model is not reliable for those stars (Youakim et al. 2017). This choice does not affect the analysis as the systemic metallicity of Sgr II is well within this range. Stars with a large uncertainty in the CaHK photometry ($\delta_{\mathrm{CaHK}} > 0.1$) are rejected. All remaining stars within $2r_{\mathrm{h}}$ are selected and their photometric metallicity distribution function (MDF) is shown in Fig. 6 as the solid red line. The distribution of all field stars within $5r_{\mathrm{h}} < r < 12r_{\mathrm{h}}$ is shown as the black dashed line for comparison.

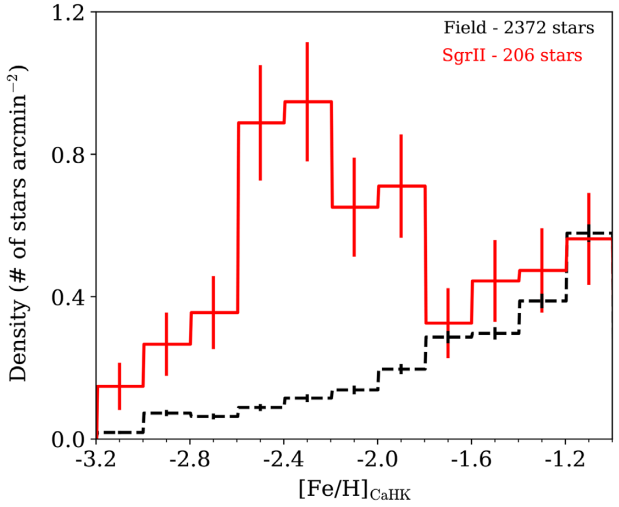

Figure 6. Normalized distribution of Pristine photometric metallicities for all stars within $2r_{\rm h}$ (solid red line). The same histogram is also shown for all field stars, i.e. stars outside $5r_{\rm h}$ (black dashed line). Sgr II clearly peaks at $[{\rm Fe/H}]_{\rm CaHK} \sim -2.3$ dex, while no such overdensity exists for the field distribution.

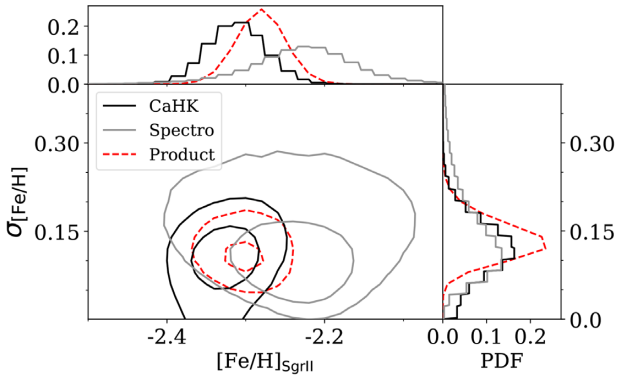

Figure 7. Two-dimensional joint PDFs of the systemic metallicity and dispersion for Sgr II using the photometric CaHK metallicities (black) and the individual spectroscopic metallicities of member stars (grey). These two independent measurements are combined to give the final PDF shown as the dashed red line. The contours represent the 39, 88, and 95 per cent volume intervals. The associated 1D marginalized PDFs for all cases are shown in the upper and right-hand panels. Both methods are in agreement and show that Sgr II has a small but measurable metallicity dispersion.

The red histogram of Sgr II stars stands out clearly in Fig. 6, with a pronounced peak around $[{\rm Fe/H}]_{\rm CaHK} \sim -2.3$ dex that does not exist in the MDF of the field stars in black. To derive Sgr II's metallicity properties, we assume that the population present inside $2r_{\rm h}$ (corresponding to 206 stars) in Fig. 6 can be modelled as the sum of the foreground MDF and a normally distributed photometric metallicity population associated with Sgr II stars. This assumption seems legitimate as the metallicity distribution at the metal-rich end of the red histogram in Fig. 6 overlaps well with the black distribution, thus implying that the underlying foreground contamination MDF is comparable over the field of view.

The Sgr II stellar population metallicity distribution is assumed to be normally distributed, with a mean $[{\rm Fe/H}]^{\rm SgrII}_{\rm CaHK}$ and a standard deviation of $\sigma = \sqrt{(\delta[{\rm Fe/H}]^{\rm CaHK}_k)^2 + (\sigma^{\rm CaHK}_{\rm [Fe/H]})^2}$, for which $\sigma^{\rm CaHK}_{\rm [Fe/H]}$ is the intrinsic metallicity dispersion of Sgr II and $\delta[{\rm Fe/H}]^{\rm CaHK}_k$ the uncertainty on the photometric metallicity of the k-th star. The likelihood model for the MW contaminating stars is built by interpolating the $[{\rm Fe/H}]_{\rm CaHK}$ MDF of all stars outside $5r_{\rm h}$. This model is then smoothed by a Gaussian kernel of 0.2 dex to account for poor statistics in some metallicity bins. The fit is performed through the same MCMC algorithm used previously, and we marginalize over the foreground contamination model. At each iteration, we randomly draw a photometric metallicity for all stars in the contamination subsample. To do so, we assume that the value of $[{\rm Fe/H}]_{\rm CaHK}$ given by the Pristine pipeline is the mean of a normal distribution, for which the uncertainty on this value, $\delta[{\rm Fe/H}]^{\rm CaHK}$, is the standard deviation. At each iteration, a new photometric metallicity is then generated for each star in the foreground contamination, thereby accounting for the uncertainty on $[{\rm Fe/H}]_{\rm CaHK}$. Then, the procedure to build the foreground contamination model described above is repeated. In doing so, the analysis takes into account the overall uncertainty of the field MDF.

The 39 and 88 per cent volume intervals on the final 2D posterior PDF, corresponding to the 1, 2, and 3σ confidence levels for the 2D Gaussian case, are shown as black solid lines in Fig. 7. We measure a significant, non-zero metallicity spread in Sgr II using only the photometric metallicities provided by Pristine, with $\sigma^{\rm SgrII}_{\rm [Fe/H]} = 0.11^{+0.05}_{-0.03}$ dex, and find it to be particularly metal-poor ($[{\rm Fe/H}]^{\rm SgrII}_{\rm CaHK} = -2.32 \pm 0.04$ dex), in agreement with the stellar population inferred through the CMD fitting. To ensure that this inference is not caused by any systematic effect, the same analysis was done in L18 with two metal-poor globular clusters in the Pristine footprint, M92 and M15. The systemic metallicities of both clusters were found to be compatible with their previous estimates using spectroscopic data. Furthermore, their metallicity dispersions were unresolved, in agreement with previous studies, showing that the technique does not seem to be affected by a systematic effect.

5 SPECTROSCOPIC ANALYSIS

5.1 Velocity properties

The systemic velocity and velocity dispersion are derived using the deep spectroscopic observations of the system, by following the procedure detailed in Section 2.2. The heliocentric velocity distributions of each individual mask are shown in the top three panels of Fig. 8. The three spectroscopic runs are combined to obtain the global velocity distribution shown in the fourth panel. Fig. 8 only shows the stars with a velocity between −400 and 0 km s^{-1} in order to have a clearer histogram in the velocity range of interest. For this reason, only 67 stars are shown in the fourth panel of the figure, but the full spectroscopic sample contains 118 stars in total. We present the radial distance of each star with respect to its radial velocity in Fig. 9, and the full data set is detailed in Tables 2 and 3.

The velocity peak of Sgr II stands out at around −177 km s^{-1} while contaminating MW stars are distributed sparsely all over the velocity space and can be located in the vicinity of the Sgr II velocity peak. Because of the small number of stars in the Sgr II population, the velocity properties can be polluted by the contamination. Ideally, those stars would have to be identified and discarded from the spectroscopic sample. Sgr II is an old and metal-poor system, as suggested by its CMD and confirmed in Sections 3, 4, and 5, whereas stars from the contaminating foreground are expected to be more metal-rich overall. Therefore, the contaminating stars could be discarded based on their metallicities. Since the spectroscopic

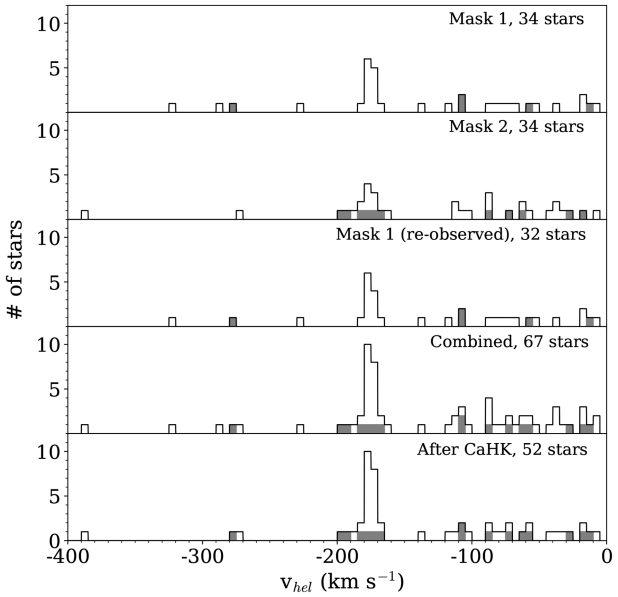

Figure 8. Heliocentric velocity histograms for the three spectroscopic samples, only for stars with a radial velocity between −400 and 0 km s^{-1}. The fourth panel shows the merging of all samples. The total number of stars in each mask is indicated in the top right corner of each panel. Two stars from mask 1 have large velocity uncertainties in the reobservation of mask 1 and were therefore discarded. Therefore, although the third panel represents a reobservation of mask 1, it does not have the same number of stars presented here. The grey histograms show the number of stars with a non-reliable photometric metallicity measurement in our sample that therefore cannot be filtered out by our technique. The peak of Sgr II stars around −177 km s^{-1} is pronounced and the disc contamination, from 0 to −100 km s^{-1}, is also quite populated. The last panel shows the final spectroscopic catalogue. 'Metal-rich' stars have been filtered out using photometric metallicities based on our CaHK photometry. For stars with reliable photometric metallicities, the ones with $-4.0 < [Fe/H]_{CaHK} < -1.6$, i.e. compatible with Sgr II metallicity properties measured in Sections 3 and 5, are selected, while the others are discarded. Stars with mediocre-quality CaHK measurement or $[Fe/H]_{CaHK}$ uncertainties are not discarded as their $[Fe/H]_{CaHK}$ is not reliable. Among the 84 stars with reliable $[Fe/H]_{CaHK}$ in the full spectroscopic sample of 118 stars, 50 are identified as part of the more metal-rich contamination and are therefore discarded.

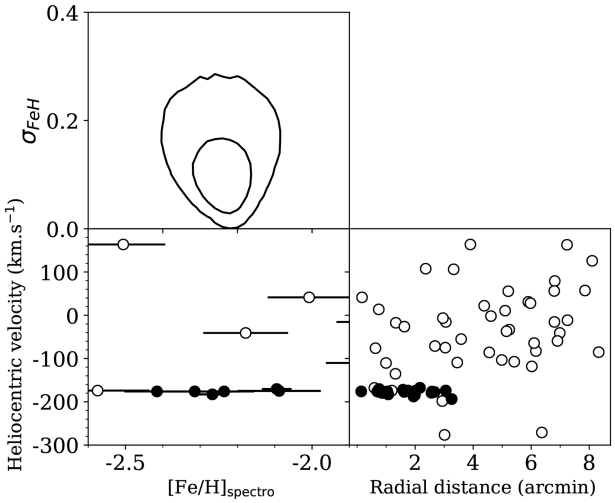

Figure 9. *Bottom right-hand panel:* radial distances to the centre of Sgr II with respect to the heliocentric velocities. Open circles represent stars that are metal-poor using their photometric metallicities, or stars with non-reliable photometric metallicity measurements. Black-filled dots represent member stars. *Bottom left-hand panel:* spectroscopic metallicities with respect to the heliocentric velocities of all stars from the final spectroscopic data set with S/N ≥ 12. *Top panel:* 2D joint PDF of the systemic spectroscopic metallicity and metallicity dispersion. The contours represent the local 39, 88, and 95 per cent volume intervals. Sgr II comes out as a very metal-poor satellite, with $[Fe/H]_{spectro} = -2.23 \pm 0.05$ dex, and seems chemically enriched: $\sigma^{spectro}_{[Fe/H]} = 0.10^{+0.06}_{-0.04}$ dex.

[Fe/H] can only be reliably measured for the brightest stars in our sample with S/N ≥12, the Pristine CaHK photometric metallicities will be used to discriminate between the MW foreground stars and the Sgr II population.

The Pristine colour–colour diagram of Sgr II is shown in Fig. 10. Field stars, i.e. a randomly selected sample of all stars outside five half-light radii, are represented as small black dots and form a clear stellar locus. This diagram is constructed so that the individual metallicity of a given star decreases from the bottom right to the top left. Stars observed with spectroscopy are colour-coded according to their heliocentric velocities, provided they have $\Delta[Fe/H]_{CaHK} < 0.5$ and $\delta_{CaHK} < 0.1$. Stars that do not match these criteria are not discarded from the final spectroscopic sample because their photometric metallicity is too uncertain to be trusted. In Section 4, we found that Sagittarius II has a systemic metallicity of $[Fe/H]^{SgrII}_{CaHK} = -2.32 \pm 0.04$ dex and has a resolved metallicity dispersion. Therefore, within the subsample of stars that passed the CaHK photometry cuts discussed above, we choose to select only stars with $-4.0 < [Fe/H]_{CaHK} < -1.6$, as a Sgr II-like system would likely have a star formation history too short to produce significantly more metal-rich stars. The region of the diagram that corresponds to such a metallicity cut is represented by the two iso-metallicity green and red lines in Fig. 10. Two cuts in $(g - i)_0$ are also applied in order to discard potential white dwarfs and metal-rich stars. The final spectroscopic velocity distribution is shown in the last panel of Fig. 8. A significant number of MW stars with reliable Pristine photometric metallicity measurements are cleaned out from the distribution as their metallicities are too high for them to be members of Sgr II, even if the satellite has a metallicity spread. In particular, one star in the immediate vicinity of the Sgr II velocity peak is identified as a more metal-rich contaminant using this technique ($[Fe/H]_{CaHK} = -1.11 \pm 0.25$ dex) and discarded.

The resulting velocity distribution is assumed to be the sum of three normally distributed populations: one for Sgr II stars and two others corresponding to the MW foreground disc and halo stars. Each individual likelihood is weighted by its CMD and structural probability membership determined in Section 5. One can write the individual likelihood of the kth star as

$$\begin{aligned}
&\mathcal{L}(\langle v_{SgrII}\rangle, \sigma_v, \langle v_{MWd}\rangle, \sigma_{vd}, \langle v_{MWh}\rangle, \sigma_{vh} | \{v_{r,k}, \delta_{v,k}\}) \\
&= \prod_k ((1 - \eta_{MWd} - \eta_{MWh}) P_{mem} G(\{v_{r,k}\} | \langle v_{SgrII}\rangle, \sigma_v) \\
&+ (1 - P_{mem})(\eta_{MWd} G(\{v_{r,k}\} | \langle v_{MWd}\rangle, \sigma_{vd}) \\
&+ \eta_{MWh} G(\{v_{r,k}\} | \langle v_{MWh}\rangle, \sigma_{vh}))), \qquad (8)
\end{aligned}$$

with $\sigma_v = \sqrt{(\sigma_v^{SgrII})^2 + \delta^2_{v,k} + \delta_{thr,i}}$ and $\delta_{v,k}$ the individual velocity uncertainty of the kth star, σ_v^{SgrII} the intrinsic velocity dispersion, δ_{thr} the systematic threshold derived in Section 2.2. $\langle v_{SgrII}\rangle$ is the systemic velocity of Sgr II. η_{MWd} and η_{MWh} are the fractions of stars respectively in the MW disc and halo populations. σ_{vd} is defined

Table 2. Properties of our spectroscopic sample. The Pristine metallicity of a given star is indicated only if $[Fe/H]_{CaHK} < -1.0$. The individual spectroscopic metallicity is reported for stars with S/N $\geq$ 12 and g_0 > 20.5 only. Stars with $P_{mem} > 0.8$ are systematically considered as members. Potential horizontal branch stars of Sgr II are marked as 'HB' as the spectroscopic pipeline extracting the velocities is less reliable for those stars. Since our CMD fitting procedure described in Section 3.1 does not account for the horizontal branch, their membership probability is not meaningful. Potential binary stars (as defined in Section 2.2) are marked as 'B'. The systematic threshold δ_{thr} is not included in the velocity uncertainties presented in this table.

RA (deg)	Dec. (deg)	g_0	i_0	$CaHK_0$	v_r (km s^{-1})	μ^*_α (mas yr^{-1})	μ_δ (mas yr^{-1})	S/N	$[Fe/H]_{CaHK}$	$[Fe/H]_{spectro}$	P_{mem}	Member
298.20599	−21.98790	18.53 ± 0.01	17.99 ± 0.01	19.44 ± 0.01	16.6 ± 1.3	2.949 ± 0.506	−6.861 ± 0.274	29.2	–	–	0.00	N
298.13158	−21.98583	19.00 ± 0.01	18.54 ± 0.01	19.77 ± 0.01	27.5 ± 1.5	−5.194 ± 0.738	−4.88 ± 0.384	22.5	–	–	0.00	N
298.13138	−21.98273	19.16 ± 0.01	18.50 ± 0.01	20.13 ± 0.01	−39.4 ± 2.2	0.336 ± 0.69	−7.317 ± 0.38	25.8	−1.39 ± 0.10	–	0.00	N
298.15508	−21.98054	19.34 ± 0.01	18.66 ± 0.01	20.52 ± 0.02	12.5 ± 1.7	1.159 ± 0.889	−8.058 ± 0.507	21.2	–	–	0.00	N
298.15097	−21.95283	19.46 ± 0.01	18.90 ± 0.01	20.39 ± 0.02	140.9 ± 1.7	−6.681 ± 1.002	0.739 ± 0.503	21.5	−1.02 ± 0.15	–	0.00	N
298.19072	−21.96758	19.88 ± 0.01	19.54 ± 0.01	20.19 ± 0.01	−118.1 ± 6.2	−0.867 ± 1.551	1.216 ± 0.81	14.4	−3.61 ± 0.17	−2.85 ± 0.23	0.00	N
298.18688	−21.97714	20.43 ± 0.01	19.87 ± 0.01	21.41 ± 0.03	−107.3 ± 2.8	−5.917 ± 2.251	−10.725 ± 1.175	12.6	–	−1.26 ± 0.13	0.00	N
298.18320	−21.96362	21.28 ± 0.01	20.73 ± 0.01	22.22 ± 0.06	−15.4 ± 3.5	– ± –	– ± –	5.6	–	–	0.30	N
298.13665	−21.97424	21.41 ± 0.01	20.90 ± 0.01	22.18 ± 0.06	−7.8 ± 7.4	– ± –	– ± –	4.7	−1.40 ± 0.30	–	0.04	N
298.19440	−21.99071	21.60 ± 0.01	21.22 ± 0.02	22.17 ± 0.06	−67.3 ± 3.8	– ± –	– ± –	3.9	−1.45 ± 0.35	–	0.00	N
298.19622	−21.99369	22.40 ± 0.02	21.66 ± 0.02	23.62 ± 0.18	−2.0 ± 13.4	– ± –	– ± –	2.8	−99.0 ± −99.0	–	0.00	N
298.16960	−22.17463	17.71 ± 0.01	16.94 ± 0.01	19.06 ± 0.01	89.7 ± 1.1	−3.409 ± 0.228	−5.191 ± 0.172	31.4	–	–	0.00	N
298.18001	−22.07175	17.90 ± 0.01	17.05 ± 0.01	19.32 ± 0.01	0.2 ± 0.9	1.896 ± 0.225	−7.431 ± 0.133	33.5	–	–	0.00	N
298.16810	−22.18830	18.27 ± 0.01	17.65 ± 0.01	19.27 ± 0.01	105.1 ± 1.3	−3.679 ± 0.287	−3.852 ± 0.18	37.2	−1.01 ± 0.11	–	0.00	N
298.19662	−22.14635	18.73 ± 0.01	18.31 ± 0.01	19.38 ± 0.01	29.2 ± 1.8	−0.708 ± 0.441	−4.393 ± 0.262	21.1	−1.30 ± 0.13	–	0.00	N
298.17484	−22.16606	18.82 ± 0.01	18.33 ± 0.01	19.65 ± 0.01	−54.0 ± 1.3	1.647 ± 0.507	−3.121 ± 0.37	27.6	–	–	0.00	N
298.19190	−22.19687	18.90 ± 0.01	18.34 ± 0.01	19.79 ± 0.01	65.8 ± 4.0	−1.137 ± 0.558	−3.422 ± 0.38	36.6	−1.15 ± 0.12	–	0.00	N
298.19827	−22.14498	18.94 ± 0.01	18.35 ± 0.01	19.77 ± 0.01	89.3 ± 1.3	−1.161 ± 0.478	−7.535 ± 0.281	25.3	−1.54 ± 0.13	–	0.00	N
298.16146	−22.08266	18.98 ± 0.01	18.20 ± 0.01	19.83 ± 0.01	−182.8 ± 0.9	−0.27 ± 0.46	−0.825 ± 0.269	26.3	−2.62 ± 0.13	−2.26 ± 0.04	0.98	Y
298.16120	−22.00829	19.04 ± 0.01	18.41 ± 0.01	20.13 ± 0.01	−85.1 ± 1.4	3.636 ± 0.626	−8.935 ± 0.343	26.7	–	–	0.00	N
298.15404	−22.11108	19.17 ± 0.01	18.71 ± 0.01	19.92 ± 0.01	51.4 ± 1.9	1.085 ± 0.593	−4.926 ± 0.335	17.5	−1.02 ± 0.15	–	0.00	N
298.15853	−22.05847	19.42 ± 0.01	19.59 ± 0.01	19.67 ± 0.01	−167.9 ± 9.5	0.865 ± 1.014	−0.73 ± 0.571	5.0	−99.0 ± −99.0	−0.44 ± 0.27	0.00	HB
298.19297	−22.02219	19.44 ± 0.01	18.93 ± 0.01	20.21 ± 0.01	122.6 ± 1.8	−0.935 ± 0.985	−1.78 ± 0.535	17.8	−1.39 ± 0.13	–	0.00	N
298.15097	−22.07939	19.56 ± 0.01	19.17 ± 0.01	19.94 ± 0.01	−174.0 ± 2.1	−1.205 ± 0.805	−0.816 ± 0.463	16.9	−3.16 ± 0.29	−2.57 ± 0.14	0.00	N
298.17764	−22.04601	19.62 ± 0.01	19.83 ± 0.01	19.63 ± 0.01	−135.3 ± 4.2	−4.001 ± 1.206	−1.43 ± 0.651	11.1	−99.0 ± −99.0	−0.92 ± 0.27	0.00	HB
298.17252	−22.07411	19.66 ± 0.01	19.90 ± 0.01	19.67 ± 0.01	−76.1 ± 10.3	−0.958 ± 1.284	−2.143 ± 0.663	11.7	−99.0 ± −99.0	−0.03 ± 0.24	0.00	HB
298.12764	−22.17289	19.75 ± 0.01	19.37 ± 0.01	20.20 ± 0.01	−15.5 ± 2.6	2.824 ± 0.831	−6.75 ± 0.504	15.0	−2.38 ± 0.29	−1.77 ± 0.16	0.00	N
298.20524	−22.02751	19.83 ± 0.01	19.01 ± 0.01	21.05 ± 0.02	201.1 ± 3.4	−3.185 ± 1.126	−15.463 ± 0.607	17.8	−1.27 ± 0.13	–	0.00	N
298.18213	−22.05709	19.85 ± 0.01	19.04 ± 0.01	21.08 ± 0.03	28.4 ± 1.8	−0.533 ± 1.135	−6.337 ± 0.594	14.9	−1.24 ± 0.12	–	0.03	N
298.14821	−22.00248	19.89 ± 0.01	19.52 ± 0.01	20.39 ± 0.02	163.6 ± 1.9	0.014 ± 1.404	−4.599 ± 0.742	14.3	−1.82 ± 0.23	−2.51 ± 0.11	0.00	N
298.16397	−22.06350	19.94 ± 0.01	19.53 ± 0.01	20.46 ± 0.02	41.4 ± 2.0	3.398 ± 1.562	−8.363 ± 0.947	14.0	−2.04 ± 0.25	−2.01 ± 0.11	0.00	N
298.16217	−22.05441	19.96 ± 0.01	19.24 ± 0.01	20.72 ± 0.02	−176.0 ± 1.5	−1.281 ± 1.022	−1.531 ± 0.539	15.8	−2.65 ± 0.16	−2.24 ± 0.08	0.99	Y
298.14762	−22.18984	20.06 ± 0.01	19.67 ± 0.01	20.63 ± 0.02	−227.3 ± 3.3	−1.419 ± 1.191	−5.42 ± 0.742	11.3	−1.57 ± 0.18	–	0.00	N
298.19401	−22.08638	20.38 ± 0.01	19.70 ± 0.01	21.09 ± 0.03	−174.9 ± 2.3	−0.305 ± 1.333	0.776 ± 0.766	13.2	−2.59 ± 0.23	−2.09 ± 0.11	0.99	Y
298.19723	−22.12452	20.51 ± 0.01	19.94 ± 0.01	21.45 ± 0.03	−323.9 ± 2.6	−10.391 ± 1.957	−3.304 ± 1.107	12.0	–	–	0.01	N
298.14902	−22.02359	20.91 ± 0.01	20.49 ± 0.01	21.45 ± 0.03	−71.1 ± 3.6	– ± –	– ± –	7.2	−2.05 ± 0.31	–	0.00	N
298.18112	−22.06077	20.93 ± 0.01	20.29 ± 0.01	21.60 ± 0.04	−179.5 ± 2.4	– ± –	– ± –	9.7	−2.54 ± 0.28	–	1.00	Y
298.17318	−22.11584	21.10 ± 0.01	20.51 ± 0.01	21.83 ± 0.04	−173.9 ± 3.8	– ± –	– ± –	6.2	−2.06 ± 0.22	–	0.97	Y
298.14955	−22.10703	21.24 ± 0.01	20.62 ± 0.01	21.89 ± 0.05	−177.4 ± 3.7	– ± –	– ± –	6.2	−2.69 ± 0.45	–	0.99	Y
298.18245	−22.10564	21.27 ± 0.01	20.67 ± 0.01	21.89 ± 0.05	−176.3 ± 6.0	– ± –	– ± –	5.6	−2.67 ± 0.36	–	0.99	Y
298.15166	−22.14928	21.54 ± 0.01	21.13 ± 0.02	22.07 ± 0.05	10.6 ± 10.6	– ± –	– ± –	4.6	−1.82 ± 0.51	–	0.00	N

Table 2 – *continued*

RA (deg)	Dec. (deg)	g_0	i_0	CaHK$_0$	v_r (km s^{-1})	μ_α^* (mas yr^{-1})	μ_δ (mas yr^{-1})	S/N	[Fe/H]$_{\rm CaHK}$	[Fe/H]$_{\rm spectro}$	$P_{\rm mem}$	Member
298.16335	−22.14322	21.60 ± 0.01	21.16 ± 0.02	22.27 ± 0.06	71.0 ± 4.9	– ± –	– ± –	4.0	−1.31 ± 0.36	–	0.00	N
298.16188	−22.05321	21.56 ± 0.01	20.99 ± 0.01	22.31 ± 0.07	−177.5 ± 7.8	– ± –	– ± –	5.7	−1.81 ± 0.37	–	1.00	Y
298.18229	−22.04275	21.61 ± 0.01	20.99 ± 0.01	22.22 ± 0.06	−177.1 ± 3.9	– ± –	– ± –	5.5	−2.96 ± 0.47	–	0.99	Y
298.19629	−22.18246	21.79 ± 0.01	21.30 ± 0.02	22.57 ± 0.08	−285.7 ± 12.8	– ± –	– ± –	4.2	−1.33 ± 0.37	–	0.02	N
298.13949	−22.1762	21.81 ± 0.01	21.41 ± 0.02	22.37 ± 0.07	174.5 ± 11.6	– ± –	– ± –	2.6	−1.49 ± 0.43	–	0.00	N
298.15003	−22.01742	21.77 ± 0.01	21.01 ± 0.01	22.59 ± 0.08	−276.5 ± 3.6	– ± –	– ± –	4.5	−2.68 ± 0.56	–	0.00	N
298.14941	−22.17937	21.82 ± 0.01	21.21 ± 0.02	22.92 ± 0.11	−59.4 ± 5.6	– ± –	– ± –	4.1	−99.0 ± −99.0	–	0.57	N
298.16383	−22.18617	21.90 ± 0.01	21.11 ± 0.02	23.39 ± 0.16	−11.5 ± 5.2	– ± –	– ± –	3.3	−99.0 ± −99.0	–	0.00	N
298.16462	−22.09165	21.93 ± 0.01	21.41 ± 0.02	22.58 ± 0.08	−172.1 ± 4.5	– ± –	– ± –	3.7	−2.05 ± 0.41	–	1.00	Y
298.17171	−22.12262	22.32 ± 0.02	21.53 ± 0.02	23.38 ± 0.16	−109.2 ± 9.5	– ± –	– ± –	3.4	−1.74 ± 0.52	–	0.00	N
298.12891	−22.15738	22.55 ± 0.02	21.04 ± 0.01	22.81 ± 0.10	31.0 ± 6.0	– ± –	– ± –	4.8	−99.0 ± −99.0	–	0.00	N
298.13975	−22.02537	22.77 ± 0.02	22.02 ± 0.03	23.42 ± 0.16	642.6 ± 13.9	– ± –	– ± –	2.4	−99.0 ± −99.0	–	0.00	N
298.16238	−22.07748	17.50 ± 0.01	16.37 ± 0.01	18.97 ± 0.01	−170.4 ± 0.7	−0.548 ± 0.158	−0.878 ± 0.087	50.6	−99.0 ± −99.0	−2.09 ± 0.04	1.00	Y
298.16425	−22.16803	17.47 ± 0.01	16.68 ± 0.01	18.82 ± 0.01	−82.8 ± 1.1	14.405 ± 0.181	−4.936 ± 0.108	38.8	−99.0 ± −99.0	−1.39 ± 0.06	0.00	N
298.29535	−22.07591	18.37 ± 0.01	17.55 ± 0.01	19.82 ± 0.01	109.3 ± 2.6	−4.564 ± 0.37	−3.604 ± 0.22	32.2	–	–	0.00	N
298.26279	−22.10197	18.50 ± 0.01	17.87 ± 0.01	19.58 ± 0.01	66.3 ± 5.3	−3.609 ± 0.38	−9.306 ± 0.209	15.3	–	–	0.00	N
298.26702	−22.08326	19.00 ± 0.01	18.54 ± 0.01	19.80 ± 0.01	11.9 ± 1.6	3.988 ± 0.662	−6.709 ± 0.369	24.3	–	–	0.00	N
298.31595	−22.06792	19.21 ± 0.01	18.70 ± 0.01	19.84 ± 0.01	−85.3 ± 2.6	2.98 ± 0.722	−7.838 ± 0.438	26.2	−2.01 ± 0.15	−1.76 ± 0.08	0.00	N
298.26878	−22.02816	19.22 ± 0.01	18.54 ± 0.01	20.39 ± 0.02	42.9 ± 1.8	−5.562 ± 0.769	−9.669 ± 0.406	24.0	–	–	0.00	N
298.28164	−22.08366	19.48 ± 0.01	18.95 ± 0.01	20.34 ± 0.02	31.1 ± 2.3	−1.95 ± 0.912	−7.823 ± 0.498	22.5	−1.01 ± 0.14	–	0.00	N
298.30703	−22.09047	19.48 ± 0.01	18.62 ± 0.01	20.98 ± 0.02	33.2 ± 3.6	−4.498 ± 0.838	0.209 ± 0.47	30.8	–	–	0.00	N
298.28935	−22.06904	19.59 ± 0.01	19.18 ± 0.01	20.19 ± 0.01	17.8 ± 1.7	1.286 ± 1.111	−5.091 ± 0.609	22.4	−1.52 ± 0.18	–	0.00	N
298.29141	−22.07521	19.68 ± 0.01	19.31 ± 0.01	20.18 ± 0.01	−40.9 ± 2.0	−2.302 ± 1.145	−11.191 ± 0.665	22.0	−1.82 ± 0.22	−2.18 ± 0.11	0.00	N
298.26110	−22.03198	19.79 ± 0.01	19.16 ± 0.01	20.86 ± 0.02	−108.8 ± 2.2	4.747 ± 1.23	−6.477 ± 0.661	21.6	–	–	0.00	N
298.27998	−22.07672	20.40 ± 0.01	19.75 ± 0.01	21.44 ± 0.03	−111.5 ± 3.2	−5.707 ± 2.05	−4.735 ± 1.075	15.6	–	–	0.49	N
298.25045	−22.08093	20.39 ± 0.01	19.57 ± 0.01	21.80 ± 0.04	73.8 ± 2.4	−4.985 ± 1.811	−11.227 ± 0.907	18.1	–	–	0.00	N
298.25661	−22.0404	20.73 ± 0.01	20.19 ± 0.01	21.42 ± 0.03	−33.3 ± 4.3	5.009 ± 3.983	−5.137 ± 2.092	10.1	−1.93 ± 0.20	–	0.00	N
298.23870	−22.10072	21.06 ± 0.01	20.60 ± 0.01	21.83 ± 0.04	−85.8 ± 5.1	– ± –	– ± –	8.4	–	–	0.00	N
298.25472	−22.05189	21.49 ± 0.01	20.99 ± 0.01	22.09 ± 0.05	−103.4 ± 5.5	– ± –	– ± –	6.5	−2.30 ± 0.40	–	0.04	N
298.31195	−22.06705	21.50 ± 0.01	20.63 ± 0.01	23.09 ± 0.12	125.8 ± 6.7	– ± –	– ± –	8.5	−99.0 ± −99.0	–	0.00	N
298.29775	−22.10044	21.77 ± 0.01	21.15 ± 0.02	22.69 ± 0.08	67.2 ± 3.8	– ± –	– ± –	5.8	−1.36 ± 0.34	–	0.35	N
298.27070	−22.09640	22.06 ± 0.01	21.22 ± 0.02	23.49 ± 0.16	−64.3 ± 7.1	– ± –	– ± –	5.7	−99.0 ± −99.0	–	0.00	N
298.28685	−22.04170	22.40 ± 0.02	21.62 ± 0.02	−0.420 ± 0.00	217.5 ± 5.7	– ± –	– ± –	3.7	−99.0 ± −99.0	–	0.00	N
298.11755	−22.07704	18.09 ± 0.01	17.49 ± 0.01	19.07 ± 0.01	21.4 ± 1.5	−2.317 ± 0.273	−2.956 ± 0.152	28.9	–	–	0.00	N
298.21458	−22.09340	18.59 ± 0.01	18.06 ± 0.01	19.63 ± 0.01	9.5 ± 2.5	−1.798 ± 0.406	−3.73 ± 0.234	25.2	–	–	0.00	N
298.15560	−22.05778	19.22 ± 0.01	18.91 ± 0.01	19.58 ± 0.01	13.6 ± 2.3	−1.788 ± 0.74	−5.022 ± 0.38	20.8	−2.71 ± 0.29	−2.8 ± 0.15	0.00	N
298.12513	−22.04616	19.24 ± 0.01	18.87 ± 0.01	19.63 ± 0.01	−179.3 ± 4.2	9.328 ± 0.675	−6.482 ± 0.376	24.2	−3.08 ± 0.27	−3.7 ± 0.33	0.00	N
298.16299	−22.08244	19.38 ± 0.01	18.61 ± 0.01	20.18 ± 0.01	−176.0 ± 1.3	−0.547 ± 0.608	−0.29 ± 0.338	26.6	−2.73 ± 0.16	−2.42 ± 0.09	0.99	Y
298.22308	−22.03976	19.52 ± 0.01	18.78 ± 0.01	20.76 ± 0.02	60.9 ± 1.9	−5.413 ± 0.935	−5.874 ± 0.519	21.5	–	–	0.92	N
298.18333	−22.07023	19.79 ± 0.01	19.33 ± 0.01	20.41 ± 0.02	−110.3 ± 2.0	7.892 ± 0.932	4.142 ± 0.541	18.4	−1.79 ± 0.19	−1.87 ± 0.1	0.00	N
298.17679	−22.05594	19.98 ± 0.01	19.16 ± 0.01	21.27 ± 0.03	−63.7 ± 2.4	2.017 ± 0.904	−9.667 ± 0.501	21.1	–	–	0.00	N
298.16641	−22.06769	20.21 ± 0.01	19.51 ± 0.01	20.95 ± 0.02	−176.0 ± 2.6	0.954 ± 1.292	0.563 ± 0.684	17.2	−2.59 ± 0.14	−2.31 ± 0.12	1.00	Y
298.17500	−22.05421	20.70 ± 0.01	20.02 ± 0.01	21.41 ± 0.03	−174.6 ± 1.7	1.235 ± 3.375	−2.706 ± 1.621	13.1	−2.66 ± 0.30	–	0.99	Y
298.20856	−22.06174	21.18 ± 0.01	20.65 ± 0.01	21.80 ± 0.04	107.6 ± 5.3	– ± –	– ± –	8.4	−2.22 ± 0.29	–	0.57	N

Table 2 – *continued*

RA (deg)	Dec. (deg)	g_0	i_0	CaHK_0	v_r (km s^{-1})	μ^*_α (mas yr^{-1})	μ_δ (mas yr^{-1})	S/N	$[\mathrm{Fe/H}]_{\mathrm{CaHK}}$	$[\mathrm{Fe/H}]_{\mathrm{spectro}}$	P_{mem}	Member
298.20446	−22.05373	21.28 ± 0.01	20.55 ± 0.01	22.41 ± 0.07	−164.6 ± 6.1	– ± –	– ± –	8.1	−1.12 ± 0.25	–	0.00	N
298.15244	−22.06164	21.31 ± 0.01	20.72 ± 0.01	21.94 ± 0.05	−177.4 ± 2.6	– ± –	– ± –	7.8	−2.50 ± 0.41	–	1.00	Y
298.19704	−22.07148	21.65 ± 0.01	21.10 ± 0.02	22.28 ± 0.06	−173.9 ± 6.0	– ± –	– ± –	6.6	−2.45 ± 0.44	–	1.00	Y
298.14088	−22.04199	21.67 ± 0.01	21.08 ± 0.02	22.38 ± 0.07	−184.7 ± 3.7	– ± –	– ± –	5.7	−2.09 ± 0.44	–	1.00	Y
298.11370	−22.07934	21.75 ± 0.01	20.93 ± 0.01	23.21 ± 0.14	−74.9 ± 5.7	– ± –	– ± –	6.9	−99.0 ± −99.0	–	0.00	N
298.13356	−22.10374	21.98 ± 0.01	21.06 ± 0.01	23.45 ± 0.17	−198.2 ± 10.4	– ± –	– ± –	5.2	−99.0 ± −99.0	–	0.00	N
298.20068	−22.05972	22.05 ± 0.01	21.50 ± 0.02	22.79 ± 0.10	−187.7 ± 5.8	– ± –	– ± –	3.8	−1.73 ± 0.41	–	1.00	Y
298.10810	−22.07218	22.07 ± 0.01	21.51 ± 0.02	22.92 ± 0.11	−193.6 ± 8.6	– ± –	– ± –	4.4	−1.45 ± 0.60	–	0.99	Y
298.19912	−22.08466	22.15 ± 0.01	21.62 ± 0.02	22.90 ± 0.10	−167.6 ± 11.5	– ± –	– ± –	3.7	−1.63 ± 0.48	–	1.00	Y
298.18916	−22.07193	22.28 ± 0.02	21.83 ± 0.02	22.86 ± 0.10	−17.5 ± 14.9	– ± –	– ± –	3.3	−2.00 ± 0.73	–	1.00	N
298.15436	−22.07078	22.30 ± 0.02	21.79 ± 0.02	22.85 ± 0.10	−171.8 ± 13.7	– ± –	– ± –	3.7	−2.72 ± 0.81	–	1.00	Y
298.14889	−22.04349	22.36 ± 0.02	21.78 ± 0.02	23.45 ± 0.17	−26.3 ± 13.5	– ± –	– ± –	3.1	−99.0 ± −99.0	–	0.99	N
298.08678	−22.10022	18.37 ± 0.01	17.60 ± 0.01	19.64 ± 0.01	18.0 ± 1.5	0.656 ± 0.279	−4.619 ± 0.163	28.0	–	–	0.00	N
298.06312	−22.0584	18.67 ± 0.01	18.19 ± 0.01	19.47 ± 0.01	16.8 ± 1.6	5.475 ± 0.404	−5.921 ± 0.228	28.9	−1.10 ± 0.12	–	0.00	N
298.08457	−22.0471	19.01 ± 0.01	18.37 ± 0.01	20.16 ± 0.01	39.1 ± 1.9	−2.449 ± 0.482	−2.806 ± 0.268	27.5	–	–	0.00	N
298.06152	−22.02591	19.30 ± 0.01	18.59 ± 0.01	20.56 ± 0.02	48.4 ± 2.4	−1.92 ± 0.559	−3.82 ± 0.317	22.1	–	–	0.01	N
298.08086	−22.0442	19.32 ± 0.01	18.79 ± 0.01	19.89 ± 0.01	−385.3 ± 1.6	−1.849 ± 0.609	−4.274 ± 0.343	23.4	−2.63 ± 0.21	−2.66 ± 0.09	0.00	N
298.08962	−22.02933	19.42 ± 0.01	18.67 ± 0.01	20.61 ± 0.02	80.2 ± 1.9	−1.374 ± 0.597	−5.162 ± 0.334	23.2	−1.03 ± 0.12	–	0.71	N
298.04697	−22.09121	19.76 ± 0.01	19.18 ± 0.01	20.34 ± 0.02	79.1 ± 2.4	−17.5 ± 0.76	−1.088 ± 0.455	22.5	−2.88 ± 0.24	−2.79 ± 0.15	0.00	N
298.07480	−22.08419	20.88 ± 0.01	19.95 ± 0.01	21.93 ± 0.05	55.5 ± 3.3	−10.032 ± 1.951	−18.831 ± 1.084	14.2	−2.62 ± 0.21	–	0.00	N
298.05488	−22.04129	20.87 ± 0.01	20.23 ± 0.01	21.93 ± 0.05	21.2 ± 5.4	1.271 ± 4.225	−12.49 ± 2.044	9.7	–	–	0.64	N
298.10189	−22.06900	20.94 ± 0.01	20.45 ± 0.01	21.52 ± 0.04	−55.2 ± 4.9	– ± –	– ± –	9.2	−2.27 ± 0.28	–	0.00	N
298.03362	−22.09989	20.97 ± 0.01	20.35 ± 0.01	21.89 ± 0.05	−85.2 ± 5.5	0.485 ± 3.664	−2.08 ± 2.111	15.5	−1.34 ± 0.21	–	0.35	N
298.05202	−22.07246	21.11 ± 0.01	20.76 ± 0.01	21.48 ± 0.04	−270.8 ± 7.6	– ± –	– ± –	7.0	−3.08 ± 0.45	–	0.00	N
298.07868	−22.07233	21.36 ± 0.01	20.79 ± 0.01	22.19 ± 0.06	21.9 ± 7.0	– ± –	– ± –	6.5	−1.53 ± 0.26	–	0.91	N
298.06683	−22.03142	21.36 ± 0.01	20.58 ± 0.01	22.71 ± 0.09	−36.9 ± 6.0	– ± –	– ± –	7.0	–	–	0.00	N
298.03617	−22.06643	21.75 ± 0.01	21.09 ± 0.01	22.78 ± 0.10	162.8 ± 6.8	– ± –	– ± –	4.6	−1.21 ± 0.45	–	0.01	N
298.02500	−22.06504	22.08 ± 0.01	21.27 ± 0.02	23.50 ± 0.18	57.2 ± 5.8	– ± –	– ± –	3.7	−99.0 ± −99.0	–	0.00	N
298.05970	−22.05248	22.40 ± 0.02	21.46 ± 0.02	−0.460 ± 0.00	27.9 ± 6.5	– ± –	– ± –	4.1	−99.0 ± −99.0	–	0.00	N
298.04913	−22.03305	17.50 ± 0.01	16.59 ± 0.01	19.05 ± 0.01	56.1 ± 1.6	4.746 ± 0.162	0.185 ± 0.092	40.1	−99.0 ± −99.0	−1.31 ± 0.08	0.00	N
298.07669	−22.08716	17.29 ± 0.01	15.89 ± 0.01	19.34 ± 0.01	−37.0 ± 1.5	−1.479 ± 0.125	−5.347 ± 0.069	44.1	−99.0 ± −99.0	−1.18 ± 0.08	0.00	N
298.21893	−22.07197	17.44 ± 0.01	16.54 ± 0.01	19.05 ± 0.01	−6.6 ± 1.7	3.183 ± 0.205	−7.464 ± 0.116	37.3	−99.0 ± −99.0	−1.18 ± 0.09	0.00	N

Table 3. Velocities and individual metallicities for all stars observed more than once, per mask. Mask 1 was observed on the 2015-09-12 and reobserved on 2015-09-18, and mask 2 on 2015-09-08 (respectively 2457283.760868, 2457277.742083, and 2457273.738102 in Julian dates). The systematic threshold $\delta_{\rm thr}$ is not included in the velocity uncertainties presented in this table. The individual spectroscopic metallicity is reported for stars with S/N $\geq$ 12 and $g_0 > 20.5$ only.

RA (deg)	Dec. (deg)	Mask	v_r (km s^{-1})	[Fe/H]$_{\rm spectro}$
298.18001	−22.07175	Combined	0.2 ± 0.9	–
		Mask 1	0.2 ± 1.6	–
		Mask 2	1.1 ± 1.7	–
		Mask 1 (reobserved)	− 0.5 ± 1.4	–
298.16146	−22.08266	Combined	− 182.8 ± 0.9	− 2.26 ± 0.04
		Mask 1	− 182.4 ± 1.8	− 2.36 ± 0.07
		Mask 2	− 183.1 ± 1.4	− 2.25 ± 0.08
		Mask 1 (reobserved)	− 182.8 ± 1.4	− 2.2 ± 0.07
298.18213	−22.05709	Combined	28.4 ± 1.8	–
		Mask 1	29.4 ± 5.6	–
		Mask 2	29.6 ± 2.4	–
		Mask 1 (reobserved)	25.7 ± 3.3	–
298.20599	−21.98790	Combined	16.6 ± 1.3	–
		Mask 1	17.4 ± 1.7	–
		Mask 1 (reobserved)	15.1 ± 2.2	–
298.13158	−21.98583	Combined	27.5 ± 1.5	–
		Mask 1	27.1 ± 2.0	–
		Mask 1 (reobserved)	28.0 ± 2.4	–
298.13138	−21.98273	Combined	− 39.4 ± 2.2	–
		Mask 1	− 44.0 ± 2.8	–
		Mask 1 (reobserved)	− 31.4 ± 3.6	–
298.15508	−21.98054	Combined	12.5 ± 1.7	–
		Mask 1	12.0 ± 2.9	–
		Mask 1 (reobserved)	12.7 ± 2.1	–
298.15097	−21.95283	Combined	140.9 ± 1.7	–
		Mask 1	140.8 ± 2.1	–
		Mask 1 (reobserved)	141.1 ± 3.1	–
298.19072	−21.96758	Combined	− 118.1 ± 6.2	− 2.85 ± 0.22
		Mask 1	− 116.0 ± 10.1	− 3.01 ± 0.26
		Mask 1 (reobserved)	− 119.4 ± 7.9	− 2.46 ± 0.41
298.18688	−21.97714	Combined	− 107.3 ± 2.8	− 1.25 ± 0.13
		Mask 1	− 114.2 ± 5.4	− 1.29 ± 0.18
		Mask 1 (reobserved)	− 104.7 ± 3.3	− 1.21 ± 0.18
298.18320	−21.96362	Combined	− 15.4 ± 3.5	–
		Mask 1	− 9.8 ± 7.3	–
		Mask 1 (reobserved)	− 17.1 ± 4.0	–
298.13665	−21.97424	Combined	− 7.8 ± 7.4	–
		Mask 1	− 1.4 ± 9.9	–
		Mask 1 (reobserved)	− 16.3 ± 11.3	–
298.19440	−21.99071	Combined	− 67.3 ± 3.8	–
		Mask 1	− 64.4 ± 7.0	–
		Mask 1 (reobserved)	− 68.5 ± 4.5	–
298.18154	−21.96963	Combined	30.1 ± 16.0	–
		Mask 1	26.3 ± 20.0	–
		Mask 1 (reobserved)	37.0 ± 26.9	–
298.19622	−21.99369	Combined	− 2.0 ± 13.4	–
		Mask 1	− 4.6 ± 17.6	–
		Mask 1 (reobserved)	1.6 ± 20.5	–
298.16960	−22.17463	Combined	89.7 ± 1.1	–
		Mask 1	88.5 ± 1.7	–
		Mask 1 (reobserved)	90.5 ± 1.5	–
298.16810	−22.18830	Combined	105.1 ± 1.3	–
		Mask 1	104.8 ± 1.5	–
		Mask 1 (reobserved)	105.9 ± 2.5	–
298.19662	−22.14635	Combined	29.2 ± 1.8	–
		Mask 1	30.8 ± 2.4	–
		Mask 1 (reobserved)	27.1 ± 2.8	–
298.17484	−22.16606	Combined	− 54.0 ± 1.3	–
		Mask 1	− 54.2 ± 1.9	–
		Mask 1 (reobserved)	− 53.9 ± 1.7	–

Table 3 – *continued*

RA (deg)	Dec. (deg)	Mask	v_r (km s^{-1})	[Fe/H]$_{\rm spectro}$
298.19827	−22.14498	Combined	89.3 ± 1.3	–
		Mask 1	91.0 ± 2.4	–
		Mask 1 (reobserved)	88.5 ± 1.6	–
298.16120	−22.00829	Combined	− 85.1 ± 1.4	–
		Mask 1	− 82.0 ± 2.1	–
		Mask 1 (reobserved)	− 87.5 ± 1.9	–
298.15404	−22.11108	Combined	51.4 ± 1.9	–
		Mask 1	51.2 ± 3.3	–
		Mask 1 (reobserved)	51.5 ± 2.4	–
298.15853	−22.05847	Combined	− 167.9 ± 9.5	− 0.46 ± 0.28
		Mask 1	− 161.0 ± 23.3	− 1.23 ± 0.77
		Mask 1 (reobserved)	− 169.3 ± 10.4	− 0.34 ± 0.31
298.19297	−22.02219	Combined	122.6 ± 1.8	–
		Mask 1	123.3 ± 2.8	–
		Mask 1 (reobserved)	122.0 ± 2.5	–
298.17764	−22.04601	Combined	− 135.3 ± 4.2	− 0.92 ± 0.28
		Mask 1	− 177.0 ± 4.9	− 1.26 ± 0.4
		Mask 1 (reobserved)	− 12.9 ± 8.4	− 0.6 ± 0.39
298.17252	−22.07411	Combined	− 76.1 ± 10.3	− 0.07 ± 0.24
		Mask 1	− 82.6 ± 18.3	− 0.07 ± 0.35
		Mask 1 (reobserved)	− 73.1 ± 12.5	− 0.08 ± 0.32
298.12764	−22.17289	Combined	− 15.5 ± 2.6	− 1.79 ± 0.16
		Mask 1	− 13.7 ± 3.4	− 1.77 ± 0.2
		Mask 1 (reobserved)	− 17.9 ± 4.0	− 1.81 ± 0.25
298.20524	−22.02751	Combined	201.1 ± 3.4	–
		Mask 1	212.3 ± 4.9	–
		Mask 1 (reobserved)	190.9 ± 4.7	–
298.14821	−22.00248	Combined	163.6 ± 1.9	− 2.5 ± 0.12
		Mask 1	163.3 ± 2.4	− 2.43 ± 0.15
		Mask 1 (reobserved)	164.1 ± 3.4	− 2.62 ± 0.2
298.16397	−22.06350	Combined	41.4 ± 2.0	− 2.02 ± 0.11
		Mask 1	42.2 ± 3.0	− 2.01 ± 0.16
		Mask 1 (reobserved)	40.7 ± 2.8	− 2.02 ± 0.16
298.16217	−22.05441	Combined	− 176.0 ± 1.5	− 2.24 ± 0.08
		Mask 1	− 176.4 ± 1.8	− 2.2 ± 0.11
		Mask 1 (reobserved)	− 175.1 ± 2.7	− 2.26 ± 0.1
298.14762	−22.18984	Combined	− 227.3 ± 3.3	–
		Mask 1	− 229.5 ± 7.4	–
		Mask 1 (reobserved)	− 226.8 ± 3.7	–
298.19401	−22.08638	Combined	− 174.9 ± 2.3	− 2.09 ± 0.11
		Mask 1	− 174.8 ± 2.7	− 2.11 ± 0.15
		Mask 1 (reobserved)	− 175.1 ± 4.4	− 2.07 ± 0.15
298.19723	−22.12452	Combined	− 323.9 ± 2.6	–
		Mask 1	− 320.8 ± 3.7	–
		Mask 1 (reobserved)	− 326.8 ± 3.6	–
298.14902	−22.02359	Combined	− 71.1 ± 3.6	–
		Mask 1	− 68.0 ± 4.1	–
		Mask 1 (reobserved)	− 80.9 ± 7.3	–
298.18112	−22.06077	Combined	− 179.5 ± 2.4	–
		Mask 1	− 179.9 ± 3.4	–
		Mask 1 (reobserved)	− 179.2 ± 3.5	–
298.17318	−22.11584	Combined	− 173.9 ± 3.8	–
		Mask 1	− 157.7 ± 6.4	–
		Mask 1 (reobserved)	− 182.8 ± 4.7	–
298.12500	−22.11766	Combined	− 179.7 ± 16.8	–
		Mask 1	− 97.2 ± 42.3	–
		Mask 1 (reobserved)	− 195.1 ± 18.3	–
298.14955	−22.10703	Combined	− 177.4 ± 3.7	–
		Mask 1	− 180.8 ± 6.1	–
		Mask 1 (reobserved)	− 175.5 ± 4.7	–
298.18245	−22.10564	Combined	− 176.3 ± 6.0	–
		Mask 1	− 172.9 ± 11.1	–
		Mask 1 (reobserved)	− 177.7 ± 7.1	–

Table 3 – *continued*

RA (deg)	Dec. (deg)	Mask	v_r (km s^{-1})	[Fe/H]$_{\rm spectro}$
298.16335	−22.14322	Combined	71.0 ± 4.9	–
		Mask 1	75.7 ± 6.8	–
		Mask 1 (reobserved)	65.8 ± 7.0	–
298.16188	−22.05321	Combined	− 177.5 ± 7.8	–
		Mask 1	− 178.1 ± 12.5	–
		Mask 1 (reobserved)	− 177.1 ± 9.9	–
298.18229	−22.04275	Combined	− 177.1 ± 3.9	–
		Mask 1	− 180.6 ± 6.3	–
		Mask 1 (reobserved)	− 175.0 ± 5.0	–
298.19593	−22.13295	Combined	22.0 ± 6.6	–
		Mask 1	− 497.1 ± 14.1	–
		Mask 1 (reobserved)	166.5 ± 7.4	–
298.13949	−22.17620	Combined	174.5 ± 11.6	–
		Mask 1	142.2 ± 24.7	–
		Mask 1 (reobserved)	183.7 ± 13.2	–
298.15003	−22.01742	Combined	− 276.5 ± 3.6	–
		Mask 1	− 273.9 ± 7.0	–
		Mask 1 (reobserved)	− 277.5 ± 4.2	–
298.14941	−22.17937	Combined	− 59.4 ± 5.6	–
		Mask 1	− 52.7 ± 6.8	–
		Mask 1 (reobserved)	− 73.5 ± 9.8	–
298.16383	−22.18617	Combined	− 11.5 ± 5.2	–
		Mask 1	− 6.4 ± 6.4	–
		Mask 1 (reobserved)	− 21.4 ± 9.0	–
298.16462	−22.09165	Combined	− 172.1 ± 4.5	–
		Mask 1	− 164.5 ± 5.5	–
		Mask 1 (reobserved)	− 189.6 ± 8.2	–
298.20290	−22.03570	Combined	− 177.4 ± 7.9	–
		Mask 1	− 181.2 ± 10.3	–
		Mask 1 (reobserved)	− 171.9 ± 12.3	–
298.17171	−22.12262	Combined	− 109.2 ± 9.5	–
		Mask 1	− 112.2 ± 17.1	–
		Mask 1 (reobserved)	− 107.9 ± 11.4	–
298.16051	−22.10941	Combined	− 51.8 ± 8.5	–
		Mask 1	− 12.1 ± 9.9	–
		Mask 1 (reobserved)	− 171.3 ± 17.1	–
298.16816	−22.18472	Combined	62.8 ± 14.7	–
		Mask 1	48.7 ± 16.5	–
		Mask 1 (reobserved)	116.8 ± 32.3	–
298.17825	−22.01529	Combined	341.2 ± 10.5	–
		Mask 1	375.7 ± 10.9	–
		Mask 1 (reobserved)	− 85.7 ± 38.3	–
298.20325	−22.11921	Combined	268.2 ± 8.4	–
		Mask 1	737.8 ± 29.0	–
		Mask 1 (reobserved)	225.0 ± 8.8	–
298.12891	−22.15738	Combined	31.0 ± 6.0	–
		Mask 1	32.6 ± 7.5	–
		Mask 1 (reobserved)	28.1 ± 9.9	–
298.18128	−22.11434	Combined	− 15.4 ± 10.0	–
		Mask 1	− 15.8 ± 14.1	–
		Mask 1 (reobserved)	− 15.0 ± 14.2	–
298.12620	−22.16308	Combined	− 100.2 ± 7.3	–
		Mask 1	− 92.8 ± 7.9	–
		Mask 1 (reobserved)	− 141.3 ± 18.6	–
298.19941	−22.10216	Combined	332.5 ± 8.3	–
		Mask 1	− 238.7 ± 19.6	–
		Mask 1 (reobserved)	457.9 ± 9.2	–
298.13975	−22.02537	Combined	642.6 ± 13.9	–
		Mask 1	574.9 ± 20.1	–
		Mask 1 (reobserved)	704.6 ± 19.2	–
298.17350	−22.09813	Combined	37.3 ± 8.2	–
		Mask 1	724.5 ± 15.4	–
		Mask 1 (re-observed)	− 238.5 ± 9.8	–

Table 3 – *continued*

RA (deg)	Dec. (deg)	Mask	v_r (km s^{-1})	[Fe/H]$_{\rm spectro}$
298.19098	−22.08826	Combined	− 305.3 ± 16.6	–
		Mask 1	− 622.7 ± 20.8	–
		Mask 1 (reobserved)	257.3 ± 27.6	–
298.14785	−22.05035	Combined	461.1 ± 10.1	–
		Mask 1	537.3 ± 26.9	–
		Mask 1 (reobserved)	448.6 ± 10.9	–
298.15192	−22.02911	Combined	126.0 ± 30.7	–
		Mask 1	139.2 ± 43.3	–
		Mask 1 (reobserved)	112.6 ± 43.6	–
298.16238	−22.07748	Combined	− 170.4 ± 0.7	− 2.09 ± 0.04
		Mask 1	− 173.2 ± 1.2	− 2.14 ± 0.06
		Mask 1 (reobserved)	− 169.0 ± 0.9	− 2.05 ± 0.06
298.16425	−22.16803	Combined	− 82.8 ± 1.1	− 1.39 ± 0.05
		Mask 1	− 83.0 ± 1.7	− 1.44 ± 0.08
		Mask 1 (reobserved)	− 82.6 ± 1.5	− 1.34 ± 0.08

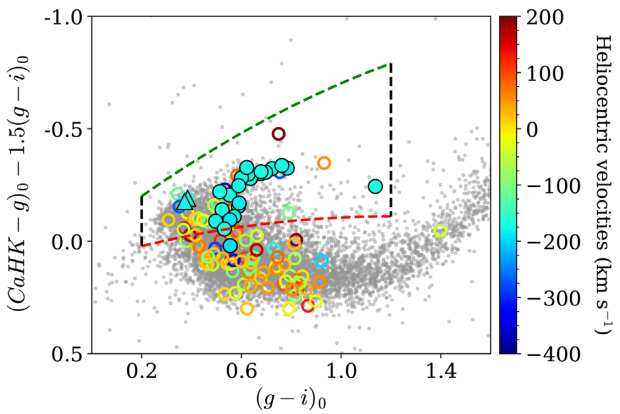

Figure 10. Pristine colour–colour diagram: The $(g - i)_0$ colour is represented on the x-axis, while the metallicity information is carried by the $(\mathrm{CaHK} - g)_0 - 1.5(g - i)_0$ colour on the y-axis. Grey dots stand for all field stars in a range between five and eight half-light radii to Sgr II. Most of them are halo and disc stars and form a stellar locus of more metal-rich stars ([Fe/H]$_{\rm CaHK} \sim 1$ or above). Stars observed with spectroscopy are represented with circles colour-coded according to their heliocentric velocities. Among those, filled circles show the stars identified as spectroscopic members, while filled triangles stand for the HB stars in the spectroscopic data set. Above the grey stellar locus are located stars that become more and more metal-poor as we go towards the upper part of the diagram. Two iso-metallicity sequences are shown in red and green dashed lines, corresponding respectively to a photometric metallicity of [Fe/H]$_{\rm CaHK} \sim$ -1.6 and [Fe/H]$_{\rm CaHK} \sim$ -4.0. As expected, most of the stars in cyan, with a radial velocity compatible with Sgr II, are located in the metal-poor region enclaved by those two sequences. Hence, only stars within this region are selected for the final spectroscopic sample. Furthermore, we add a criterion on $(g - i)_0$ and discard all stars outside $0.2 < (g - i)_0 < 1.2$ in order to discard potential foreground white dwarfs.

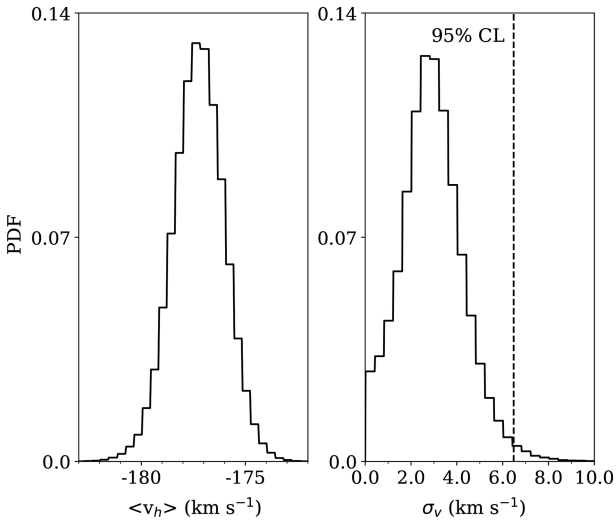

Figure 11. Marginalized PDFs for the systemic velocity (left) and its associated dispersion (right) for Sgr II. The satellite is found to be dynamically cold. The velocity dispersion is only marginally resolved: $\sigma_{\rm vr} = 2.7^{+1.3}_{-1.0}$ km s^{-1}, reaching 6.5 km s^{-1} at the 95 per cent confidence level.

as $\sigma_{\rm vd} = \sqrt{(\sigma_{\rm v}^{\rm MWd})^2 + \delta_{{\rm v},k}^2 + \delta_{{\rm thr},i}}$, with $\sigma_{\rm v}^{\rm MWd}$ the intrinsic velocity dispersion of the disc population. The corresponding quantity for the halo population is written $\sigma_{\rm vh}$, while $\langle v_{\rm MWd} \rangle$ is the systemic velocity of the disc population in the sample (resp. for the halo population). G is the usual 1D normal distribution. We run an MCMC analysis and show the resulting marginalized 1D PDFs in Fig. 11. At each iteration of the MCMC, the systematic threshold $\delta_{\rm thr}$ is randomly drawn from its PDF. The favoured systemic velocity is $\langle v_{\rm SgrII} \rangle = -177.3 \pm 1.2$ km s^{-1}. The velocity dispersion of Sgr II is $\sigma_{\rm v}^{\rm SgrII} = 2.7^{+1.3}_{-1.0}$ km s^{-1}, reaching 6.5 km s^{-1} at the 95 per cent confidence interval, thus showing that Sagittarius II is a dynamically cold satellite. A similar analysis was performed for the inner ($r < 1$ arcmin) and outer ($r > 1$ arcmin) regions and no statistical difference was found in terms of velocity dispersion, with $\sigma_v^{\rm inner} = 2.1^{+1.6}_{-1.4}$ and $\sigma_v^{\rm outer} = 2.9^{+2.1}_{-1.4}$ km s^{-1}. Using these inferences as well and taking into account the CMD and spatial models derived in Section 3, 21 stars are identified as members of Sgr II.

5.2 Metallicity properties

To infer the metallicity properties of Sgr II from the spectrocopy, we create a subsample constituted of stars brighter than $i_0 = 20.5$ and an S/N ratio above 12 from our final spectroscopic sample, for a total of 26 stars. The spectroscopic metallicity is estimated using the calibration from Starkenburg et al. (2010; hereafter S10) based on the Ca triplet. This method is originally calibrated for RGB stars above the horizontal branch; however, Leaman et al. (2013) showed

that it can be applied to stars up to two magnitudes fainter (see also Carrera et al. 2013).

The spectroscopic metallicity uncertainties come from the respective uncertainties on each parameters used in the calibration of S10. The uncertainties on the measurements of the equivalent widths (EWs) of the calcium triplet lines are provided by our pipeline. The latter uses the EWs of the calcium triplet and an absolute magnitude. For each star, we assume that the uncertainty on each EW is Gaussian. Therefore, a value of each EW is drawn from a normal distribution, with a mean being the favoured EW inferred from our pipeline, and a standard deviation corresponding to its uncertainty. The photometric and distance modulus uncertainties are also folded in the uncertainty of the absolute magnitude M_I used in the calibration. In the uncertainty on M_I is included the one coming from the transformation from the PS1 photometric system to the one used by S10 in their calibration, following Tonry et al. (2012). The randomly drawn EWs, $m - M$, and M_I are then used to compute a spectroscopic metallicity. We perform this task 10 000 times to obtain a PDF of the spectroscopic metallicity for each star, and derive from there the favoured $[\mathrm{Fe/H}]_{\mathrm{spectro}}$ and its uncertainties. Six out of these 26 stars have a membership probability greater than 90 per cent and are also dynamical members of Sgr II. Among those six stars, the lowest S/N is 17. They constitute our final sample to infer the systemic metallicity of the satellite. The other 20 are discarded. The individual spectroscopic metallicities are reported in Table 2 under '$[\mathrm{Fe/H}]_{\mathrm{spectro}}$'. The distribution of spectroscopic metallicities with respect to the radial velocity is shown in the bottom left-hand panel of Fig. 9, and shows the existence of a clump of stars at around $[\mathrm{Fe/H}]_{\mathrm{spectro}} \sim -2.3$ dex at the velocity of Sgr II.

To derive the systemic metallicity and metallicity dispersion of Sgr II, we assume that the spectroscopic metallicities of Sgr II stars are normally distributed and weigh each star with its CMD and structural probability membership, giving the following likelihood function:

$$\mathcal{L}(\langle[\mathrm{Fe/H}]_{\mathrm{spectro}}\rangle, \sigma_{[\mathrm{Fe/H}]} | \{[\mathrm{Fe/H}]_{\mathrm{spectro},k}, \delta_{[\mathrm{Fe/H}],k}) = P_{\mathrm{mem}}\, G([\mathrm{Fe/H}]_{\mathrm{spectro},k}, \delta_{[\mathrm{Fe/H}],k} | \langle[\mathrm{Fe/H}]_{\mathrm{spectro}}\rangle, \sigma_{[\mathrm{Fe/H}]}\}), \quad (9)$$

with $\sigma_{[\mathrm{Fe/H}]} = \sqrt{\delta^2_{[\mathrm{Fe/H}],k} + (\sigma^{\mathrm{sgr}}_{[\mathrm{Fe/H}]})^2}$, $\delta_{[\mathrm{Fe/H}],k}$ the individual uncertainty on the spectroscopic metallicity of the kth star, and $\sigma^{\mathrm{sgr}}_{[\mathrm{Fe/H}]}$ the intrinsic metallicity dispersion of Sgr II. The 39, 88, and 95 per cent volume intervals are represented by black solid lines on the resulting 2D PDFs in the top left-hand panel of Fig. 9. Sgr II is confirmed to be metal-poor, with $[\mathrm{Fe/H}]^{\mathrm{SgrII}}_{\mathrm{spectro}} = -2.23 \pm 0.05$ dex. Moreover, we find a metallicity dispersion of $\sigma^{[\mathrm{Fe/H}]}_{\mathrm{spectro}} = 0.10^{+0.06}_{-0.04}$ dex. This spread in metallicity is driven by the two brightest stars identified as members of Sgr II, for which the spectroscopic metallicity is accurately measured. They have a spectroscopic metallicity of -2.27 ± 0.04 and -2.10 ± 0.04 dex, respectively. Furthermore, since they are among the stars that were observed multiple times in our catalogue, it is possible to infer their individual spectroscopic metallicities using the Ca triplet EWs of each run separately. For both stars, the metallicities obtained from each spectroscopic run in which they were observed are consistent. The first star has been observed three times, with metallicity measurements of $[\mathrm{Fe/H}]^1_{\mathrm{spectro}} = -2.36 \pm 0.07$, $[\mathrm{Fe/H}]^2_{\mathrm{spectro}} = -2.25 \pm 0.08$, and $[\mathrm{Fe/H}]^3_{\mathrm{spectro}} = -2.20 \pm 0.07$ dex. The second star has two metallicity measurements, $[\mathrm{Fe/H}]^1_{\mathrm{spectro}} = -2.14 \pm 0.06$ and $[\mathrm{Fe/H}]^2_{\mathrm{spectro}} = -2.05 \pm 0.06$ dex. This suggests that their final [Fe/H] are not driven by one spurious EW measurement in one of the three spectroscopic samples. In addition to being consistent with the CMD of Sgr II and its systemic velocity, the two stars are also remarkably compatible with the satellite's proper motion inferred in Section 6. Taken all together, we favour the fact that these two stars are indeed members of Sgr II, and that there is a spread in metallicity in the system.

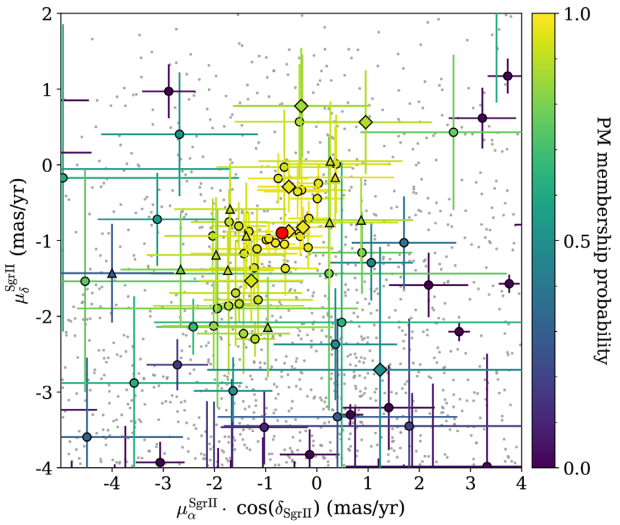

Figure 12. Distribution of the proper motions of MW contaminating stars in small grey dots, and our Sgr II-like population shown with dots colour-coded according to their proper motion membership probability, derived from a Gaussian mixture model. The 7 Sgr II members with a proper motion measurement in *Gaia* are represented with diamonds and the12 HB stars with triangles. The systemic proper motion of Sgr II ($\mu^*_\alpha = -0.65^{+0.08}_{-0.10}$ mas yr^{-1}, $\mu_\delta = -0.88 \pm 0.12$ mas yr^{-1}) is represented with a large red dot.

The two measurements of the metallicity and dispersion of the satellite, using the CaHK observations on the one hand and the spectra on the other, are perfectly compatible. In order for the two measurements to be independent, the stars used to infer the spectroscopic metallicity properties are discarded from the photometric metallicity sample before inferring $[\mathrm{Fe/H}]_{\mathrm{CaHK}}$ and σ_{CaHK}. The product of the 2D joint PDFs is then performed and the results of both methods are combined into one single measurement. We show the corresponding 39, 88, and 95 per cent volume intervals as red thick lines in Fig. 7. This final measurement yields a systemic metallicity of $[\mathrm{Fe/H}]_{\mathrm{SgrII}} = -2.28 \pm 0.03$ dex and a metallicity dispersion of $\sigma^{\mathrm{SgrII}}_{[\mathrm{Fe/H}]} = 0.12^{+0.03}_{-0.02}$ dex.

6 *GAIA* DR2 PROPER MOTIONS AND ORBIT

To infer the orbit of Sgr II, we first build a sample of possible Sgr II stars based on the mask shown in the right-hand panel of Fig. 2. The proper motions of those stars are retrieved from the *Gaia* Data Release 2 (Gaia Collaboration 2018a). All member stars identified as members from our spectroscopy and bright enough to have a proper motion measurement in *Gaia* are naturally present in this sample. Furthermore, the *Gaia* DR2 data are also cross-matched with the potential HB stars within two half-light radii of the satellite. Twelve HB stars have a proper motion measurement in *Gaia* and are added to the sample shown in Fig. 12.

The inference of the Sgr II proper motion is performed through a Gaussian mixture model. We assume that the sample can be modelled by the sum of two bivariate Gaussians: one for the Sgr II population and another for the foreground MW contamination.

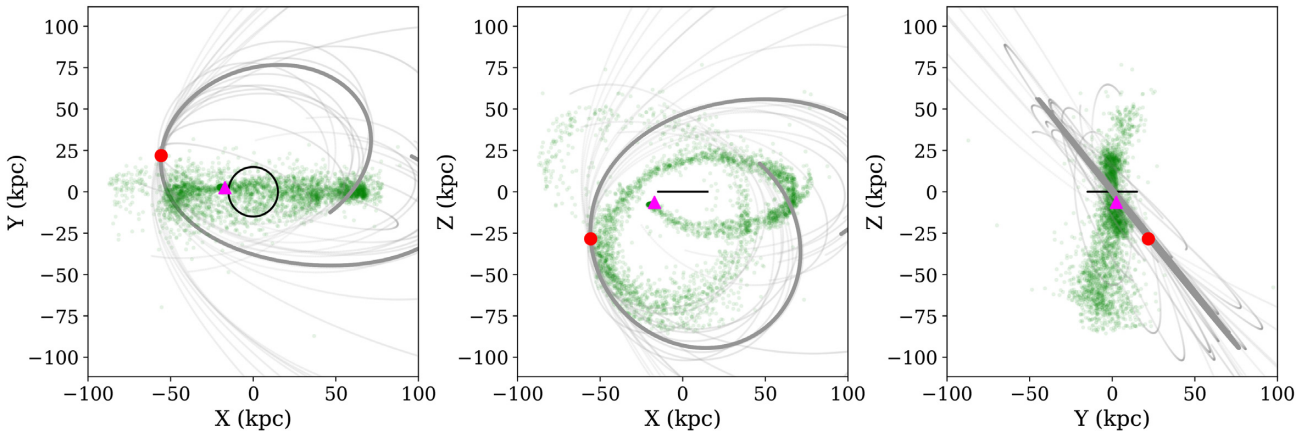

Figure 13. Projections of the orbit of Sgr II on the *X*–*Y*, *X*–*Z*, and *Y*–*Z* planes backwards and forwards over 2.0 Gyr. Twenty-one orbits are shown here: the one based on the favoured position, distance, radial velocity, and proper motion of the satellite (as the thick, darker grey line), and twenty others using random realizations of those parameters (as thin, slightly transparent grey lines). The red circle is the current position of Sgr II, while the magenta triangle is the one of the Sgr dSph. An *N*-body simulation of the trailing arm of the Sgr stream (Law & Majewski 2010) is shown in green. The MW disc is shown in black, with a chosen radius of 15 kpc.

The sets of parameters inferred from the analysis are composed of the proper motions in both directions, their dispersions and correlation c, for Sgr II ($\mathcal{P}_{\rm SgrII} = \langle\mu^*_{\alpha,\rm SgrII}\rangle, \langle\mu_{\delta,\rm SgrII}\rangle, \sigma_1, \sigma_2, c_{\rm SgrII}$) and for the contamination ($\mathcal{P}_{\rm MW} = \langle\mu^*_{\alpha,\rm MW}\rangle, \langle\mu_{\delta,\rm MW}\rangle, \sigma_3, \sigma_4, c_{\rm MW}$). The proper motion properties of the kth star are defined as $\vec{d}_k = \{\mu^*_{\alpha,k}, \mu_{\delta,k}, \delta\mu^*_{\alpha,k}, \delta\mu_{\delta,k}\}$ with $\delta\mu^*_{\alpha,k}$ the uncertainty on the proper motion in the RA direction (respectively the DEC direction). The likelihood of the kth star is

$$\mathcal{L}(\mathcal{P}_{\rm SgrII}, \mathcal{P}_{\rm MW}|\vec{d}_k) = \prod_k \eta P_{mem} \mathcal{M}_{\mathcal{G}}(\vec{d}_k|\mathcal{P}_{\rm SgrII}, \mathcal{P}_{\rm MW}) + (1-\eta)(1-P_{mem})\mathcal{M}_{\mathcal{G}}(\vec{d}_k|\mathcal{P}_{\rm SgrII}, \mathcal{P}_{\rm MW}), \quad (10)$$

where $\mathcal{M}_{\mathcal{G}}$ is a 2D Gaussian and η the fraction of Sgr II stars in the sample.

The Gaussian mixture model gives a systemic proper motion of $\mu_\alpha^{*,\rm SgrII} = -0.65^{+0.08}_{-0.10}$ and $\mu_\delta^{\rm SgrII} = -0.88 \pm 0.12$ mas yr^{-1} for Sgr II. These proper motions take into account the systematic error derived by the Gaia Collaboration (2018b). We also inferred the proper motion of the system using the HB and spectroscopic member stars only, and found a compatible result with $(\mu^*_\alpha, \mu_\delta) = (-0.55 \pm 0.13, -0.80 \pm 0.08)$ mas yr^{-1}.

Our estimate is discrepant from the one of Massari & Helmi (2018), who find a proper motion of $(\mu^*_\alpha, \mu_\delta) = (-1.18 \pm 0.14, -1.14 \pm 0.11)$ mas yr^{-1}. They rely on the convergence of the astrometric parameters through a 2.5σ clipping procedure, with an initial guess on those parameters based on the potential HB stars of Sgr II. However, our measurement based only on HB and spectroscopic member stars gives credit to the proper motion found in our work, and disfavours the estimate of the work of Massari & Helmi (2018), which might be biased by the foreground contamination.

The orbit of the satellite can then be inferred using the GALPY package (Bovy 2015). The MW potential chosen to integrate the orbit is a modified 'MWPotential14' constituted of three main components: a power-law, exponentially cut-off bulge, a Miyamoto–Nagai Disc, and an NFW DM halo with a virial mass of 1.2×10^{12} M$_\odot$. Further details about this MW potential model can be found in Bovy (2015). We integrate 2000 orbits backwards and forwards, each time by randomly drawing a position, distance, radial velocity, and proper motions from their respective PDFs, and extract for each realization the pericentre, apocentre, and ellipticity of the orbit, integrated over 2 Gyr. The favoured orbit (i.e. the favoured position, distance, radial velocity, and proper motions) is shown in Fig. 13 in the *X*–*Y*, *X*–*Z*, and *Y*–*Z* planes, along with the stream from the Sgr dwarf galaxy. Twenty other random realizations of Sgr II orbits are also shown in grey, partially transparent lines.

The analysis yields a pericentre of $54.8^{+3.3}_{-6.1}$ kpc, an apocentre of $118.4^{+28.4}_{-23.7}$ kpc, and an orbital ellipticity of 0.44 ± 0.01. Moreover, Fig. 13 shows that the orbit of Sgr II is compatible with the trailing arm of the Sgr stream, despite being slightly tilted from it, especially in the *Y* direction.

7 DISCUSSION

We used deep MegaCam broad-band photometry, data from the narrow-band CaHK Pristine survey, and DEIMOS spectroscopy to conduct a thorough study of the Milky Way satellite Sgr II. By performing a CMD and structural analysis, the satellite is found to have a half-light radius of $35.5^{+1.4}_{-1.2}$ pc, and is located at a distance of $73.1^{+1.1}_{-0.7}$ kpc based on the combination of BHB stars' distances and a CMD fitting procedure. The favoured stellar population is old (12.0 ± 0.5 Gyr) and metal-poor. Using our spectroscopic catalogue, we are able to find the systemic velocity of Sgr II to be $\langle v_{\rm SgrII}\rangle = -177.3 \pm 1.3$ km s^{-1}. The velocity dispersion yields $\sigma_{\rm v}^{\rm sgr} = 2.7^{+1.3}_{-1.0}$ km s^{-1} and is smaller than 6.5 km s^{-1} at the 95 per cent confidence interval. From the spectroscopic analysis, 21 stars are identified as members of the satellite and reported in Table 2. The individual photometric metallicities provided by the Pristine survey are used to show that Sgr II is a very metal-poor system, with $[{\rm Fe/H}]^{\rm SgrII}_{\rm CaHK} = -2.32 \pm 0.04$ dex, and has a small but resolved metallicity dispersion: $\sigma^{\rm CaHK}_{\rm [Fe/H]} = 0.11^{+0.05}_{-0.03}$ dex. These two chemical properties are perfectly supported by our spectroscopic analysis of six RGB stars. We applied the Ca triplet calibration from S10 to member stars to derive the spectroscopic metallicity of Sgr II and its associated dispersion: $[{\rm Fe/H}]^{\rm SgrII}_{\rm spectro} = -2.23 \pm -0.08$ dex and $\sigma^{\rm CaHK}_{\rm [Fe/H]} = 0.10^{+0.06}_{-0.04}$ dex. Combining the CaHK and spectroscopic measurements, we obtain refined estimates of both parameters: $[{\rm Fe/H}]_{\rm SgrII} = -2.28 \pm 0.04$ dex and $\sigma^{\rm SgrII}_{\rm [Fe/H]} = 0.12^{+0.03}_{-0.02}$

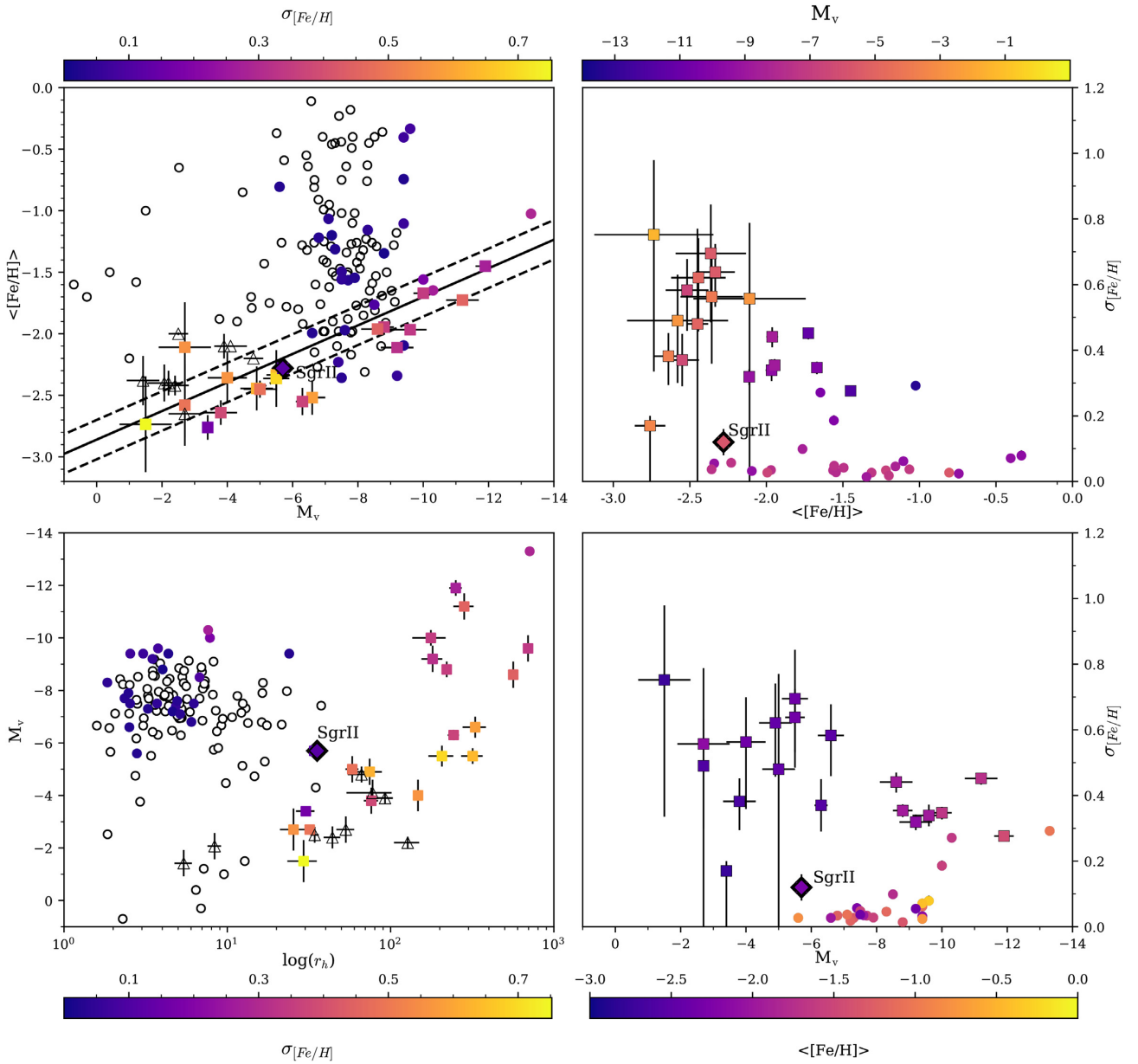

Figure 14. Comparison of Sgr II with other GCs and dwarf galaxies of the Milky Way. Squares represent dwarf galaxies while circles represent globular clusters, and the diamond corresponds to Sgr II. Triangles stand for recently discovered dwarf-galaxy candidates that await confirmation. Hollow markers correspond to systems for which no metallicity dispersion measurement can be found in the literature. The solid line in the top left-hand panel corresponds to the luminosity–metallicity relation of Kirby et al. (2013) for dwarf spheroidals and dwarf irregulars. Dashed lines represent the RMS about this relation, also taken from Kirby et al. (2013). Among the 123 globular clusters presented here, the properties of 116 were extracted from the Harris (1996) catalogue, revised in 2010. For the remaining ones (Kim 1, Kim 2, Kim 3, Laevens 1, Balbinot 1, Munoz 1, and SMASH 1) parameters of the discovery publications were used (Muñoz et al. 2012; Balbinot et al. 2013; Laevens et al. 2014; Kim et al. 2015; Kim & Jerjen 2015; Kim et al. 2016; Martin et al. 2016b). Globular cluster metallicity spread measurements are taken from Willman & Strader (2012) and references therein: Carretta et al. (2006), Carretta et al. (2007), Carretta et al. (2009), Carretta et al. (2011), Cohen et al. (2010), Gratton et al. (2007), Johnson & Pilachowski (2010), and Marino et al. (2011). McConnachie (2012) and Willman & Strader (2012) are used to compile the properties of the dwarf galaxies represented here. The 18 dwarf galaxies represented here are Bootes I (Belokurov et al. 2006; Norris et al. 2010), Canes Venatici I (Zucker et al. 2006b), Canes Venatici II (Sakamoto & Hasegawa 2006), Coma Berinices, Hercules, Leo IV and Segue I (Belokurov et al. 2007), Draco and Ursa Minor (Wilson 1955), Fornax (Shapley 1938b), Leo I and Leo II (Harrington & Wilson 1950), Pisces II (Belokurov et al. 2010), Sculptor (Shapley 1938a), Sextans (Irwin et al. 1990), Ursa Major I (Willman et al. 2005b), Ursa Major II (Zucker et al. 2006a), and Willman I (Willman et al. 2005a). Their metallicity and metallicity spreads were drawn from Kirby et al. (2008), Kirby et al. (2010), Norris et al. (2010), and Willman et al. (2011). The dwarf galaxy candidates discovered recently and shown on this figure are Bootes II (Koch & Rich 2014), DES1 (Luque et al. 2016; Conn et al. 2018), Eridanus III (Bechtol et al. 2015; Koposov et al. 2015b; Conn et al. 2018), Hyades II (Martin et al. 2015), Pegasus III (Kim & Jerjen 2015), Reticulum II and Horologium I (Koposov et al. 2015a), Segue II (Belokurov et al. 2009), and the most significant candidates of Drlica-Wagner et al. (2015): Gru II, Tuc III, and Tuc IV.

dex. Finally, using the *Gaia* DR2 data, the proper motion of Sgr II is inferred to be $(\mu_\alpha^*, \mu_\delta) = (-0.65^{+0.08}_{-0.10}, -0.88 \pm 0.12)$ mas yr^{-1}. This yields an apocentre and pericentre of $118.4^{+28.4}_{-23.7}$ and $54.8^{+3.3}_{-6.1}$ kpc, respectively.

Sgr II is in perfect agreement with the luminosity–metallicity relation for dwarf galaxies (Kirby et al. 2013), as is shown in the top left-hand panel of Fig. 14. Sgr II is however somewhat of an outlier in the r_h–M_V plane (bottom left-hand panel of Fig. 14), which led M18 to conclude that Sgr II is a globular cluster. However, the locus of dwarf galaxies in this plane becomes uncertain at low luminosities. The satellite is still more extended than the vast majority of MW globular clusters, as shown in the bottom left-hand panel of Fig. 14, although two of them have a comparable size: Crater (Belokurov et al. 2014; Laevens et al. 2014) and Terzan 5 (Terzan 1968). These two extended clusters do not, however, share the same metallicity properties as Sgr II: Terzan 5 is a bulge cluster with [Fe/H] > -0.5 and Crater is more metal-rich, with a systemic metallicity of [Fe/H] ~ -1.65 (Weisz et al. 2016). Our two estimates of the metallicity dispersion of Sgr II both yield similar results and suggest that the satellite was able to retain its gas and form successive generation of stars, thus suggesting the presence of a dark matter halo (Willman & Strader 2012). Inferring the metallicity dispersion with the calcium triplet calibration of Carrera et al. (2013; hereafter C13), specifically built for very metal-poor stars, yields $\sigma^{C13}_{[Fe/H]} = 0.20^{+0.10}_{-0.05}$ dex. However, these results have to be taken with care. First of all, they are driven by only two bright RGB stars that have significantly different metallicity measurements. If one of the two were misidentified as an Sgr II member, the claim of a metallicity dispersion would be weaker. Moreover, the uncertainties on the spectroscopic metallicities of the brightest stars in our sample compare with the ones reachable with high-resolution spectroscopy, indicating that they are unrealistically low. No systematics is explicitly specified in S10, but they mention an 8 per cent maximum error on the fitted parameters of their relation. When this systematic threshold is applied, the metallicity dispersion of Sgr II is unresolved ($<$0.34 dex at the 95 per cent confidence level). C13 specify the uncertainties of each fitted parameters of their relation, which are taken into account in the inference of $\sigma^{C13}_{[Fe/H]}$ above. The discrepancy between the results from S10 and C13 implies that there may be an unquantified systematic error that impacts our measurement of the metallicity dispersion, and could therefore weaken our conclusion on the nature of Sgr II. Finally, another possible source of systematic error would be the [Ca/Fe] ratio, which is not necessarily constant in this metallicity regime. The existence of a calcium abundance dispersion in Sgr II would also impact the inferred metallicity dispersions from calcium triplet calibration techniques. For these reasons, even though we are able to identify two member stars with discrepant metallicity measurements in the satellite using two different calcium triplet calibration techniques, one should remain careful about the existence of a metallicity dispersion in Sgr II.

The question of the dynamical mass of Sgr II remains open. We can use the relation of Walker et al. (2009) to estimate the expected velocity dispersion of a purely baryonic system. Assuming a mass-to-light ratio of 2 for an old and metal-poor stellar population (McLaughlin & van der Marel 2005), Sgr II would have a velocity dispersion of ~ 1 km s^{-1}, which is not incompatible with our inference of $\sigma_{vr} = 2.7^{+1.3}_{-1.0}$ km s^{-1}. Never the less, taken at face value, our velocity dispersion measurement implies that Sgr II has a dynamical mass-to-light ratio of $23.0^{+32.8}_{-23.0}$ $M_\odot\ {L_\odot}^{-1}$ and favours a slightly DM-dominated system under the usual assumption of dynamical equilibrium and sphericity. If this is confirmed, it would mean that Sgr II inhabits one of the lowest mass DM subhaloes. Alternatively, this result could be driven by the compactness of the satellite, whose stars only probe the inner parts of the subhalo.

Taken together, these two pieces of evidence (marginally resolved metallicity dispersion and plausibly non-baryonic mass-to-light ratio) would indicate that Sgr II is more likely a dwarf galaxy rather than a cluster.

Before the submission of this work, a spectroscopic study of Sgr II was presented at the AAS iPoster[2] session (Simon et al. 2019). Using *Magellan*/IMACS spectroscopy, they found a systemic velocity and metallicity compatible to the ones in this work: $\langle v_r \rangle = -177.3 \pm 0.7$ km s^{-1} and $\langle$[Fe/H]$\rangle = -2.28$ dex. Their velocity dispersion is also consistent with ours: $\sigma_{vr} = 1.6 \pm 0.3$ km s^{-1}. Finally, the proper motion they derive for Sgr II ($(\mu_\alpha^*, \mu_\delta) = (-0.63^{+0.08}_{-0.10}, -0.89 \pm 0.06$ mas yr^{-1}) is also perfectly in agreement with our work. However, they estimate a very low metallicity dispersion, with $\sigma_{[Fe/H]} < 0.08$ dex at the 95 per cent confidence limit. Therefore, they conclude that the satellite is a globular cluster. Once the two data sets are made public, a thorough investigation is needed to understand the source of this discrepancy, which could be the unquantified systematics in the calcium triplet calibration procedures discussed earlier. Anyhow, it illustrates the difficulty of studying and understanding such faint systems.

Independently of the nature of Sgr II, the orbit we infer for the satellite is compatible with the trailing arm of the Sagittarius stream according to the model by Law & Majewski (2010) (Fig. 13). However, we note that the agreement between the two orbits is not perfect and, in particular, that the position of Sgr II today and its favoured movement in the *Y*–*Z* galactocentric plane are slightly offset from the plane of the Sgr stream. Three hypotheses can be formulated to explain this discrepancy:

(i) The fact that the Sgr stream and the Sgr II orbits are compatible is purely coincidental.

(ii) Sgr II is linked to the stream, and the discrepancy between Sgr II and the stream in the *Y* direction, if real, could be explained by the fact that Sgr dSph satellites were stripped first and with a different energy than that of stars represented in the simulation.

(iii) Sgr II is linked to the stream and is also representative of its behaviour around the MW. No model is able to match all the observational constraints existing for the Sgr stream (Fardal et al. 2019), so the observed difference in the orbital plane of Sgr and Sgr II could suggest that the behaviour of the distant Sgr stream wrap that Sgr II would be associated with is not perfectly described by the Law & Majewski (2010) simulation.

If either the second or the third scenario is the valid one, it would mean that Sgr II is a new, exciting example of of a satellite. Similarly to the Magellanic Clouds, the Sgr dSph would then have brought its own cohort of satellites that have now been deposited in the MW halo. Moreover, it would also bring some precious insights on the orbit of the Sgr stream in regions where it is poorly constrained.

ACKNOWLEDGEMENTS

We gratefully thank the CFHT staff for performing the observations in queue mode, for their reactivity in adapting the schedule, and for answering our questions during the data-reduction process. We thank Nina Hernitschek for granting us access to her Pan-STARRS1 variability catalogue.

[2] <https://aas233-aas.ipostersessions.com/default.aspx?s = E7-10-7C-92-5D-B1-84-24-1F-B5-07-1A-BF-2E-10-65>

ES, KY, and AA gratefully acknowledge funding by the Emmy Noether programme from the Deutsche Forschungsgemeinschaft (DFG). This work has been published under the framework of the IdEx Unistra and benefits from a funding from the state managed by theFrench National Research Agency as part of the investments for the future program. NFM, RI, and NL gratefully acknowledge support from the French National Research Agency (ANR) funded project 'Pristine' (ANR-18-CE31-0017) along with funding from CNRS/INSU through the Programme National Galaxies et Cosmologie and through the CNRS grant PICS07708. The authors thank the International Space Science Institute (ISSI), Berne, Switzerland for providing financial support and meeting facilities to the international team 'Pristine'. JIGH acknowledges financial support from the Spanish Ministry project MINECO AYA2017-86389-P, and from the Spanish MINECO under the 2013 Ramón y Cajal program MINECO RYC-2013-14875.

BPML gratefully acknowledges support from FONDECYT postdoctoral fellowship No. 3160510.

Based on observations obtained at the Canada–Franc—Hawaii Telescope (CFHT) which is operated by the National Research Council of Canada, the Institut National des Sciences de l'Univers of the Centre National de la Recherche Scientifique of France, and the University of Hawaii.

Some of the data presented herein were obtained at the W. M. Keck Observatory, which is operated as a scientific partnership among the California Institute of Technology, the University of California, and the National Aeronautics and Space Administration. The Observatory was made possible by the generous financial support of the W. M. Keck Foundation. Furthermore, the authors wish to recognize and acknowledge the very significant cultural role and reverence that the summit of Maunakea has always had within the indigenous Hawaiian community. We are most fortunate to have the opportunity to conduct observations from this mountain.

The Pan-STARRS1 Surveys (PS1) have been made possible through contributions of the Institute for Astronomy, the University of Hawaii, the Pan-STARRS Project Office, the Max-Planck Society and its participating institutes, the Max Planck Institute for Astronomy, Heidelberg, and the Max Planck Institute for Extraterrestrial Physics, Garching, The Johns Hopkins University, Durham University, the University of Edinburgh, Queen's University Belfast, the Harvard-Smithsonian Center for Astrophysics, the Las Cumbres Observatory Global Telescope Network Incorporated, the National Central University of Taiwan, the Space Telescope Science Institute, the National Aeronautics and Space Administration under Grant No. NNX08AR22G issued through the Planetary Science Division of the NASA Science Mission Directorate, the National Science Foundation under Grant No. AST-1238877, the University of Maryland, and Eotvos Lorand University (ELTE).

This work has made use of data from the European Space Agency (ESA) mission *Gaia* (https://www.cosmos.esa.int/gaia), processed by the *Gaia* Data Processing and Analysis Consortium (DPAC, https://www.cosmos.esa.int/web/gaia/dpac/consortium). Funding for the DPAC has been provided by national institutions, in particular the institutions participating in the *Gaia* Multilateral Agreement.

REFERENCES

Balbinot E. et al., 2013, ApJ, 767, 101
Bechtol K. et al., 2015, ApJ, 807, 50
Belokurov V. et al., 2006, ApJ, 647, L111
Belokurov V. et al., 2007, ApJ, 654, 897
Belokurov V. et al., 2009, MNRAS, 397, 1748
Belokurov V. et al., 2010, ApJ, 712, L103
Belokurov V., Irwin M. J., Koposov S. E., Evans N. W., Gonzalez-Solares E., Metcalfe N., Shanks T., 2014, MNRAS, 441, 2124
Bernard E. J. et al., 2014, MNRAS, 442, 2999
Bertone G., Hooper D., Silk J., 2005, Phys. Rep., 405, 279
Boulade O. et al., 2003, SPIE, 4841, 72
Bovy J., 2015, ApJS, 216, 29
Boylan-Kolchin M., Bullock J. S., Kaplinghat M., 2011, MNRAS, 415, L40
Bullock J. S., Boylan-Kolchin M., 2017, ARA&A, 55, 343
Carrera R., Pancino E., Gallart C., del Pino A., 2013, MNRAS, 434, 1681
Carretta E., Bragaglia A., Gratton R. G., Leone F., Recio-Blanco A., Lucatello S., 2006, A&A, 450, 523
Carretta E. et al., 2007, A&A, 464, 967
Carretta E. et al., 2009, A&A, 505, 117
Carretta E., Lucatello S., Gratton R. G., Bragaglia A., D'Orazi V., 2011, A&A, 533, A69
Chambers K. C. et al., 2016, preprint (arXiv:1612.05560)
Cohen J. G., Kirby E. N., Simon J. D., Geha M., 2010, ApJ, 725, 288
Conn B. C., Jerjen H., Kim D., Schirmer M., 2018, ApJ, 852, 68
Deason A. J., Belokurov V., Evans N. W., 2011, MNRAS, 416, 2903 (D11)
Dotter A., Chaboyer B., Jevremović D., Kostov V., Baron E., Ferguson J. W., 2008, ApJS, 178, 89
Drlica-Wagner A. et al., 2015, ApJ, 813, 109
Faber S. M. et al., 2003, SPIE, 4841, 1657
Fardal M. A., van der Marel R. P., Law D. R., Sohn S. T., Sesar B., Hernitschek N., Rix H.-W., 2019, MNRAS, 483, 4724
Gaia Collaboration, Brown A. G. A., Vallenari A., Prusti T., de Bruijne J. H. J., Babusiaux C., Bailer-Jones C. A. L., 2018a, SPIE, 616, 22
Gaia Collaboration et al., 2018b, A&A, 616, A12
Geringer-Sameth A., Koushiappas S. M., Walker M., 2015, ApJ, 801, 74
Gratton R. G. et al., 2007, A&A, 464, 953
Harrington R. G., Wilson A. G., 1950, PASP, 62, 118
Harris W. E., 1996, AJ, 112, 1487
Hastings W. K., 1970, Biometrika, 97
Ibata R., Sollima A., Nipoti C., Bellazzini M., Chapman S. C., Dalessandro E., 2011, ApJ, 738, 186
Ibata R. A., Gilmore G., Irwin M. J., 1994, Nature, 370, 194
Irwin M., Lewis J., 2001, New Astron. Rev., 45, 105
Irwin M. J., Bunclark P. S., Bridgeland M. T., McMahon R. G., 1990, MNRAS, 244, 16P
Johnson C. I., Pilachowski C. A., 2010, ApJ, 722, 1373
Joo S.-J. et al., 2019, ApJ, 875, 2
Kim D., Jerjen H., 2015, ApJ, 799, 73
Kim D., Jerjen H., Milone A. P., Mackey D., Da Costa G. S., 2015, ApJ, 803, 63
Kim D., Jerjen H., Mackey D., Da Costa G. S., Milone A. P., 2016, ApJ, 820, 119
Kirby E. N., Simon J. D., Geha M., Guhathakurta P., Frebel A., 2008, ApJ, 685, L43
Kirby E. N. et al., 2010, ApJS, 191, 352
Kirby E. N., Cohen J. G., Guhathakurta P., Cheng L., Bullock J. S., Gallazzi A., 2013, ApJ, 779, 102
Koch A., Rich R. M., 2014, ApJ, 794, 89
Koposov S. E., Yoo J., Rix H.-W., Weinberg D. H., Macciò A. V., Escudé J. M., 2009, ApJ, 696, 2179
Koposov S. E. et al., 2011, ApJ, 736, 146
Koposov S. E., Belokurov V., Torrealba G., Evans N. W., 2015a, ApJ, 805, 130
Koposov S. E. et al., 2015b, ApJ, 811, 62
Laevens B. P. M. et al., 2014, ApJ, 786, L3
Laevens B. P. M. et al., 2015a, ApJ, 813, 44
Laevens B. P. M. et al., 2015b, ApJ, 802, L18
Law D. R., Majewski S. R., 2010, ApJ, 714, 229
Leaman R. et al., 2013, ApJ, 767, 131
Longeard N. et al., 2018, MNRAS, 480, 2609
Luque E. et al., 2016, MNRAS, 458, 603

Marino A. F. et al., 2011, A&A, 532, A8
Martin N. F., Ibata R. A., Irwin M. J., Chapman S., Lewis G. F., Ferguson A. M. N., Tanvir N., McConnachie A. W., 2006, MNRAS, 371, 1983
Martin N. F. et al., 2015, ApJ, 804, L5
Martin N. F. et al., 2016a, ApJ, 833, 167
Martin N. F. et al., 2016b, ApJ, 830, L10
Massari D., Helmi A., 2018, A&A, 620, A155
Mateo M. L., 1998, ARA&A, 36, 435
McConnachie A. W., 2012, AJ, 144, 4
McLaughlin D. E., van der Marel R. P., 2005, ApJS, 161, 304
Muñoz R. R., Geha M., Côté P., Vargas L. C., Santana F. A., Stetson P., Simon J. D., Djorgovski S. G., 2012, ApJ, 753, L15
Mutlu-Pakdil B. et al., 2018, ApJ, 863, 25 (M18)
Navarro J. F. et al., 2010, MNRAS, 402, 21
Norris J. E., Wyse R. F. G., Gilmore G., Yong D., Frebel A., Wilkinson M. I., Belokurov V., Zucker D. B., 2010, ApJ, 723, 1632
Pawlowski M. S., McGaugh S. S., Jerjen H., 2015, MNRAS, 453, 1047
Pawlowski M. S. et al., 2017, Astron. Nachr., 338, 854
Sakamoto T., Hasegawa T., 2006, ApJ, 653, L29
Schlafly E. F., Finkbeiner D. P., 2011, ApJ, 737, 103
Schlegel D. J., Finkbeiner D. P., Davis M., 1998, ApJ, 500, 525
Sesar B. et al., 2017, AJ, 153, 204 (S17)
Shapley H., 1938a, Harvard College Observatory Bulletin, 908, 1
Shapley H., 1938b, Nature, 142, 715
Simon J., Fu S. W., Geha M., Kelson D. D., Alarcon Jara A. G., 2019, American Astronomical Society Meeting Abstracts, #233
Simon J. D., Geha M., 2007, ApJ, 670, 313
Starkenburg E. et al., 2010, A&A, 513, A34 (S10)
Starkenburg E. et al., 2017, MNRAS, 471, 2587
Terzan A., 1968, Comptes Rendus B, 267, 1245
The Dark Energy Survey Collaboration, 2005, preprint (astro-ph/0510346)
Tonry J. L. et al., 2012, ApJ, 750, 99
Tulin S., Yu H.-B., 2018, PhR, 730, 1
Walker M. G., Mateo M., Olszewski E. W., Peñarrubia J., Wyn Evans N., Gilmore G., 2009, ApJ, 704, 1274
Weisz D. R. et al., 2016, ApJ, 822, 32
Willman B., Strader J., 2012, AJ, 144, 76
Willman B. et al., 2005a, AJ, 129, 2692
Willman B. et al., 2005b, ApJ, 626, L85
Willman B., Geha M., Strader J., Strigari L. E., Simon J. D., Kirby E., Ho N., Warres A., 2011, AJ, 142, 128
Wilson A. G., 1955, PASP, 67, 27
Wolf J., Martinez G. D., Bullock J. S., Kaplinghat M., Geha M., Muñoz R. R., Simon J. D., Avedo F. F., 2010, MNRAS, 406, 1220
York D. G. et al., 2000, ApJ, 120, 1579
Youakim K. et al., 2017, MNRAS, 472, 2963
Zucker D. B. et al., 2006a, ApJ, 650, L41
Zucker D. B. et al., 2006b, ApJ, 643, L103

[1]*Université de Strasbourg, CNRS, Observatoire astronomique de Strasbourg, UMR 7550, F-67000 Strasbourg, France*
[2]*Max-Planck-Institut für Astronomy, Königstuhl 17, D-69117 Heidelberg, Germany*
[3]*Leibniz Institute for Astrophysics Potsdam (AIP), An der Sternwarte 16, D-14482 Potsdam, Germany*
[4]*Department of Physics, University of Surrey, Guildford, GU2 7XH Surrey, UK*
[5]*Department of Astronomy, Yale University, New Haven, CT 06520, USA*
[6]*Institute of Astrophysics, Pontificia Universidad Católica de Chile, Av. Vicuna Mackenna 4860, 7820436 Macul, Santiago, Chile*
[7]*Research School of Astronomy and Astrophysics, Australian National University, Canberra, ACT 2611, Australia*
[8]*University of California Los Angeles, Department of Physics & Astronomy, Los Angeles, CA 90095, USA*
[9]*Institute of Astronomy, University of Cambridge, Madingley Road, Cambridge CB3 0HA, UK*
[10]*GEPI, Observatoire de Paris, PSL Research University, CNRS, Place Jules Janssen, F-92190 Meudon, France*
[11]*Laboratoire d'astrophysique, École Polytechnique Fédérale de Lausanne (EPFL), Observatoire, CH-1290 Versoix, Switzerland*
[12]*Instituto de Astrofisica de Canarias, Via Lactea, E-38205 La Laguna, Tenerife, Spain*
[13]*Departamento de Astrofisica, Universidad de La Laguna, E-38206 La Laguna, Tenerife, Spain*
[14]*Department of Physics and Astronomy, University of Victoria, P.O. Box 3055, STN CSC, Victoria, BC V8W 3P6, Canada*
[15]*NRC Herzberg Astronomy and Astrophysics, 5071 West Saanich Road, Victoria, BC V9E 2E7, Canada*
[16]*Royal Observatory Edinburgh, Blackford Hill, Edinburgh EH9 3HJ, UK*

This paper has been typeset from a TEX/LATEX file prepared by the author.